NASA TECHNICAL MEMORANDUM

NASA TM X-1123

NASA TM X-1123

THE EXPLORER XXIII MICROMETEOROID SATELLITE

DESCRIPTION AND PRELIMINARY RESULTS FOR THE PERIOD NOVEMBER 6, 1964 THROUGH FEBRUARY 15, 1965

Compiled by Robert L. O'Neal
Langley Research Center
Langley Station, Hampton, Va.

NATIONAL AERONAUTICS AND SPACE ADMINISTRATION • WASHINGTON, D. C. • AUGUST 1965

NASA TM X-1123

THE EXPLORER XXIII MICROMETEOROID SATELLITE

DESCRIPTION AND PRELIMINARY RESULTS FOR THE PERIOD NOVEMBER 6, 1964 THROUGH FEBRUARY 15, 1965

Compiled by Robert L. O'Neal

Langley Research Center
Langley Station, Hampton, Va.

NATIONAL AERONAUTICS AND SPACE ADMINISTRATION

For sale by the Clearinghouse for Federal Scientific and Technical Information
Springfield, Virginia 22151 – Price $3.00

THE EXPLORER XXIII MICROMETEOROID SATELLITE

DESCRIPTION AND PRELIMINARY RESULTS FOR THE PERIOD

NOVEMBER 6, 1964 THROUGH FEBRUARY 15, 1965

Compiled by Robert L. O'Neal
Langley Research Center

31142

SUMMARY

The Explorer XXIII (1964 74A) is in orbit with a perigee of 250 nautical miles and an apogee of 529 nautical miles. It carries stainless-steel pressurized cells, impact detectors, capacitor detectors, cadmium sulfide cells, and test solar cells.

The puncture rate in 0.002-inch stainless steel, derived on the basis of 25 punctures received to date, is 0.017 $ft^{-2}day^{-1}$. With 95-percent confidence, the average puncture rate in 0.002-inch stainless steel lies between 0.011 and 0.025 puncture $ft^{-2}day^{-1}$.

The puncture rate in 0.001-inch stainless steel, derived on the basis of 24 punctures received to date, is 0.036 $ft^{-2}day^{-1}$. With 95-percent confidence, the average puncture rate in 0.001-inch stainless steel lies between 0.023 and 0.053 puncture $ft^{-2}day^{-1}$.

The puncture rates obtained for stainless steel on Explorer XXIII are close to the puncture rates obtained from beryllium-copper on Explorer XVI. The confidence limits easily include the data points obtained from Explorer XVI.

No counts have been recorded by the capacitor-detector experiment through December 19, 1964. No measurable degradation of the test solar cells has been observed through December 19, 1964. Counting rates on the high-sensitivity impact-detection system (>0.03 dyne-sec) have averaged lower than rates measured by the high-sensitivity system (>0.5 dyne-sec) on Explorer XVI. The cadmium sulfide cell meteoroid-penetration experiments were found to be inoperative immediately after launch.

Telemeter performance was satisfactory throughout this reporting period. Telemeter and battery temperatures and temperatures of all experiments have remained within acceptable limits.

author

INTRODUCTION

Explorer XXIII (1964 74A), previously designated the S-55c micrometeoroid satellite, was placed in orbit on November 6, 1964 by the Scout launch vehicle. The primary objective of the experiment is to collect statistically significant micrometeoroid-penetration-rate data in two thicknesses of stainless steel. The secondary objective is to collect data on the effects of the space environment on the operation of a capacitor-type meteoroid-penetration detector. Other objectives are to obtain data on meteoroid impacts in three momentum ranges, to obtain data on punctures produced in 1/8-mil and 1/4-mil poly[ethylene terephthalate] film (PET) by micrometeoroids, and to obtain data on the degradation of n/p solar cells in the space environment. The Explorer XXIII program is planned to provide information which will supplement that obtained from the micrometeoroid satellite Explorer XVI. Results from that program are given in references 1 to 4.

The purpose of this report is to present some of the data obtained during the initial weeks of operation of Explorer XXIII. Micrometeoroid-penetration-rate data presented covers the time period from launch through February 15, 1965. The data presented for the other experiments cover the time period from launch through December 19, 1964. The report is thus preliminary in nature. Much of the information in reference 1 describing the spacecraft, systems, and operations has been used directly in this report when pertinent to the Explorer XXIII.

The various parts of the Explorer XXIII program are under several different experimenters and specialists who have contributed much of the text in this report relating to their particular areas. Mr. Earl C. Hastings, Jr. is project manager. The experimenters and specialists and the parts of the program with which they are involved are as follows:

Contributor	Contribution
James Bene	Test solar-cell experiment
Charles A. Gurtler and Gary W. Grew	Pressurized-cell experiment
Dale G. Holden and Alfred G. Beswick	Meteoroid impact detection experiment
Wendell H. Lee	Orbital elements and spacecraft motions
Luc Secretan	Cadmium sulfide cell experiment
James H. Siviter, Jr.	Capacitor-detector development and experiment
Doyle P. Swofford	Thermal control system
Leon V. Taylor	Telemetry system

All are associated with the Langley Research Center except Mr. Secretan, who is associated with the Goddard Space Flight Center.

DESCRIPTION OF SPACECRAFT AND EXPERIMENTS

Figure 1 is a photograph of Explorer XXIII, and figure 2 is a sketch showing the spacecraft in the vehicle heat shield. Principal dimensions and arrangement of systems on the spacecraft are also shown. The spacecraft was built around the fourth-stage motor of the launch vehicle, and the burned-out fourth stage remained as part of the orbiting satellite. The spacecraft is cylindrical in shape, about 24 inches in diameter, and about 92 inches long. Spacecraft weight, the vehicle fourth-stage hardware and motor being neglected, is 212 lb. The weight of the assembly placed in orbit after fourth-stage burnout is 296 lb. Three types of sensors are used to obtain information regarding micrometeoroids. These sensors, as noted in figure 2, are pressurized cells, impact detectors, and cadmium sulfide cells.

Pressurized Cells

The pressurized cells, developed at the Langley Research Center, are the primary sensors onboard the spacecraft. The sensors are made of type 302 stainless steel. Figure 3 is a drawing of the pressurized-cell detector. A total of 216 of the pressure cells are mounted in seven rows around the periphery of the spacecraft. Each row contains 32 cells except the forward row which contains 24. The telemeter system could not accommodate 6 of the cells and, as a result, these 6 cells are inactive and do not record penetrations. Each cell is filled with helium; when the cell is punctured, the gas leaks out and the pressure loss actuates a switch, the opening of which indicates the puncture. Thus, after one puncture, the cell cannot indicate additional punctures; however, the open switch does provide permanent storage of the information that the cell is punctured. A thermal balance coating was applied to the outer surface of each pressurized cell. It consisted of a coating of silicon monoxide over a base coating of aluminum. Dr. Georg Hass and Alan P. Bradford of U.S. Army Engineer Research and Development Laboratories, Ft. Belvoir, Virginia, directed the coating application.

A cross-sectional view of some of the pressure cells mounted around the periphery of the spacecraft is shown in figure 4. This placement of the cells is typical of the six most forward rows with the exception of the first row where 4 cells are omitted from each side to provide space for mounting the two capacitor detectors. In each of the six forward rows of cells there is an 0.08-inch gap between adjacent cells, except for four 0.44-inch gaps equally spaced around the periphery of the spacecraft. In the aft row of cells, where the spacecraft diameter is increased by 0.80 inch, these gaps are 0.14 inch and 0.52 inch.

The area exposed to the influx of micrometeoroids in space is considered to be π times the diameter of the circumscribed circle (22.90 inches for the six forward rows and 24.15 inches for the aft row) multiplied by the detector sensing length of the detectors, a correction being made for the open area between the sensors. This definition of area gives a total value of 22.2 square feet for the prelaunch condition. The area associated with each sensor is 0.106 square foot. This area is used in all analyses connected with the

pressure-cell experiment. The areas corresponding to the various thicknesses are given in the following table:

Table I

External skin thickness, in.	Number of active cells	Area, sq ft
0.001	70	7.4
.002	140	14.8

Capacitor Detector

The capacitor type of meteoroid-penetration detector being flown on the Explorer XXIII is being developed by the Langley Research Center. This sensor is essentially a thin-film capacitor made up of a thin-film polymer dielectric with a stainless-steel-foil target plate serving as one electrode and a vacuum-deposited copper film serving as the opposite electrode. When a high-energy particle penetrates the charged capacitor, a significant amount of material is vaporized and ionized in the area of the penetration. As a result, the capacitor is momentarily shorted and discharges. The momentary change of the voltage across the sensor during this discharge is detected and stored. The ionization dissipates in less than 1 microsecond and allows the capacitor to recharge. The detector should thus be capable of sensing any number of punctures unlike the pressurized cells which can sense only the first puncture.

The target plate or penetration material is 0.001-inch type 302 stainless steel, which is the same as the material used in the 0.001-inch pressure cells. Figure 5 is a photograph of the sensor and figures 6 and 7 show the sensor configuration and cross section, respectively. Each of the two sensors on the spacecraft has an exposed area of 0.391 square foot. A more detailed description and discussion of the capacitor detector is given in the appendix.

The temperature of the sensor is determined from a thermistor element located on the rear surface of a 3/4 inch by 1/4 inch sensor sample constructed similar to the sensor, except for size, and placed adjacent to it. The temperature-sensing sample is shown in figure 6.

The purpose of the capacitor detector on the Explorer XXIII is to determine whether the space-radiation environment has any adverse effects on the operation of the capacitor as a meteoroid-penetration detector. Ground tests have indicated that this environment may cause spurious discharges of the capacitor. A more detailed discussion of these tests and the results is given in the appendix.

Impact-Detection System

The micrometeoroid-impact-detection system consists of 24 triangular sounding boards. Each board has an area of 0.064 square foot; thus, the total exposed area is 1.54 square feet. Figure 8 shows a sketch of a typical impact

detector. The sounding boards are made of 0.051-inch-thick 6061 aluminum alloy and are coated for thermal control. All the sounding boards are slightly curved in order to fit around the periphery of the spacecraft.

A piezoelectric element is attached to the underside of each board, and the boards are so mounted that they are acoustically isolated from the rest of the spacecraft structure. The sounding boards are electrically arranged in four groups. Six sounding boards are electrically paralleled to form each group. The impact event signals from the four groups are sent to an amplifier which equalizes the sensitivity of each of the groups. The four groups, in effect, function as one transducer and the different threshold levels are selected electronically. The system is threshold sensitive to three levels of impact momentum; that is, only impacts above a certain momentum level are recognized and recorded.

The three sensitivity levels were determined by dropping small spheres of known mass from various heights on to the sounding board and noting for each sensitivity level the height which will just produce an output from the system. The three sensitivity levels were calculated to be 0.03 dyne-second, 0.8 dyne-second, and 12 dyne-seconds for the high-, medium-, and low-sensitivity ranges, respectively.

Cadmium Sulfide Cells

The cadmium sulfide cell detector was developed by the Goddard Space Flight Center. A drawing of this detector is shown in figure 9. The detector consists of a light-sensitive cadmium sulfide element mounted beneath a sheet coated with PET film and having evaporated aluminum on both sides. The useful surface area is about 0.037 square foot per cell. Penetration of the aluminized PET-coated sheet will allow sunlight (direct or reflected) to illuminate the cadmium sulfide cell element and reduce its resistance. This resistance change is monitored by the telemeter system. Two of these cells are on the forward face of the spacecraft. One is mounted beneath a sheet of 1/4-mil PET film and one is mounted beneath a sheet of 1/8-mil PET film.

Test Solar Cells

Four test groups of n/p silicon solar cells and an aspect sensor, which are located on the forward face of the spacecraft, make up the solar-cell degradation experiment. Two of the test groups are unprotected and two are covered with 3/16-inch fused quartz as shown in figure 10. Each test group consists of 5 single 1 by 2 centimeter cells, series connected in a shingle. Each shingle is loaded with a resistor, the voltage across which is monitored.

An aspect sensor is used to provide the orientation data necessary to evaluate the test solar-cell results properly. The aspect sensor consists of six triangular silicon solar cells arranged in a hexagon. The cells are illuminated through and protected by a 1/4-inch fused-quartz window. The illuminated area of the cells is a circle of approximately $\frac{21}{32}$-inch diameter. Each cell is resistance loaded individually, and the six cells are connected together in series. The output of the device is a voltage which is dependent upon the angle that the spacecraft makes with the sun.

Telemetry System

The telemetry system for the Explorer XXIII consists of two separate and independent telemeters for telemetering the data, and a radio beacon for initial tracking of the satellite. The various sensors are divided into two groups as nearly equal as possible and are telemetered separately. Any given sensor is connected only to one system so that the same piece of information is telemetered only once, but the division is made so that the same types of information are transmitted by both systems. Accordingly, if one telemeter fails, the entire experiment will not be lost, but the exposed area for each type of experiment will be halved. The telemetry system is mounted on a bulkhead inside the nose section of the spacecraft.

The two telemeters are of the data-storage, command-readout type wherein data are collected during orbit and read out when within range of a Minitrack data-acquisition station. Data readout is nondestructive so that noisy receptions can be discarded and the data obtained by later readouts. It was necessary to use two frequency links for data transmission, but only one frequency is used for commanding the readout.

The two telemeters are constructed as independently as possible. Separate solar cells and batteries are used to supply power to each telemeter. Redundancy is provided in the command system by connecting the two command receivers so that either command receiver can turn on both telemeters. A common antenna system is used for both telemeters, but the two telemeters are connected through a hybrid junction in order to be electrically isolated.

A block diagram of the telemetry system is shown in figure 11. The pertinent characteristics are presented in the following table:

Table II

	Type	Emission	Frequency, Mcps	Power output, mW	Life-time, days	Power supply
Telemeter A	Pulse duration modulation/frequency modulation/amplitude modulation; 48 channels	30A9 for 1 minute, upon interrogation only	136.080	500	365	Secondary batteries (Ni-Cd) recharged by solar cells
Telemeter B	Pulse duration modulation/frequency modulation/amplitude modulation; 48 channels	30A9 for 1 minute, upon interrogation only	136.860	500	365	Secondary batteries (Ni-Cd) recharged by solar cells
Radio beacon	Master oscillating power amplifier	0A0	136.860	150	7	Primary batteries (Hg)

ORBIT ELEMENTS AND SPACECRAFT MOTIONS

Explorer XXIII was launched on November 6, 1964, at 12:02:01 Greenwich mean time (GMT) (07:02:01 EST) on a Scout launch vehicle, and was injected into orbit at 12:11:15 GMT. Nominal orbital elements computed before launch are shown in the following table along with the initial orbital elements measured on November 6, 1964, and updated to December 10, 1964.

Table III

Parameter	Nominal (prelaunch)	Measured as of Nov. 6, 1964	Measured as of Dec. 10, 1964
Perigee altitude, n. mi.	247.46	250.37	250.53
Apogee altitude, n. mi.	539.78	529.32	528.44
Inclination, deg	51.99	51.95	51.95
Period, min	99.16	99.23	99.23

At injection the spacecraft was spinning about the longitudinal axis which was inclined at an angle of approximately 25° to the sun.

Prior to fourth-stage ignition, the motor and payload were spun about the longitudinal axis by means of four spin motors. No subsequent despin was employed. Signal-strength records taken at Antigua, BWI, (near the injection point) were used to determine spin rates. Results are presented in the following table which covers a period from just after spinup until after fourth-stage burnout.

Table IV

Description of relative time placement of spin rate	Time interval over which spin rate was determined, GMT	Spin rate, rpm
Between spinup and fourth-stage ignition . . .	12:10:46.37 to 12:10:50.52	144 ± 1
Near middle of fourth-stage burning	12:11:02.97 to 12:11:07.11	145 ± 1
Near end of fourth-stage burning	12:11:12.0 to 12:11:16.0	150 ± 1
First point after fourth-stage burnout	12:11:18.42 to 12:11:22.82	150 ± 1
Second point after fourth-stage burnout	12:13:04.90 to 12:13:08.92	149 ± 1
Third point after fourth-stage burnout	12:18:06.62 to 12:18:10.62	150 ± 1

The data in table IV show an increase in spin rate during the fourth-stage burning. Although this increase cannot be predicted accurately, it is expected as a result of momentum transfer between propellant and motor during the fourth-stage burning. The spin rate of 144 rpm after spinup was much lower than the predicted nominal value of 165 rpm. Inaccuracy in the determination of the moment of inertia used to predict the spin rate could not account for this difference. Possible causes of the discrepancy are (a) one or more of the spin motors may not have performed as expected, and (b) the spin-table bearing

friction might have been higher than expected. Figure 12 shows the spin rates about the longitudinal axis which have been measured to date. The spin rates at injection were determined by using the antenna nulls of the received-signal-strength records and recorded range time. The accuracy of these measurements is ±1 rpm. The spin rates existing after injection were determined by using the antenna nulls of the received-signal-strength records and a locally generated time. The use of this locally generated time limits the accuracy to ±5 rpm.

Figure 13 shows a plot of cone angle for the satellite during this period of transition from spinning about its axis of minimum moment of inertia to tumbling about its axis of maximum moment of inertia. Figure 13 was calculated simply by making the cosine of the cone angle equal to the ratio of the spin rate to the initial spin rate. Inaccuracies in the spin rate also cause corresponding inaccuracies in the cone angle, which become very large when the cosine of the cone angle is close to 1. The dotted lines in figure 13 show the accuracy bands corresponding to the ±5 rpm spin-rate accuracy.

RESULTS AND DISCUSSION

Pressurized-Cell Experiment

Twenty-five of the 140 pressurized-cell detectors with 0.002-inch stainless-steel test material have been punctured during the first 108 days of orbital lifetime. This puncture rate corresponds to an average puncture rate of 0.017 puncture $ft^{-2}day^{-1}$. During this same period of time, 24 of the 70 pressurized-cell detectors with 0.001-inch stainless-steel test material have been punctured, the puncture rate corresponding to an average puncture rate of 0.036 puncture $ft^{-2}day^{-1}$.

Experimental data for the pressurized cells have been taken from 474 interrogations, the last of which was on the 1573rd pass. Of these interrogations, 332 contained data from both telemeters and 142 interrogations contained data from only 1 of the telemeters. As previously indicated, the pressure-cell detectors are divided into two groups which are telemetered separately on the two telemeters. One telemeter transmits data on seventy 0.002-inch detectors and forty 0.001-inch detectors. The other telemeter transmits data on seventy 0.002-inch detectors and thirty 0.001-inch detectors. When only one of the telemetric transmissions from an interrogation is reducible, data are received, in effect, from only approximately one-half of the sensors. Data are not lost in such cases, since they can be recovered in subsequent interrogations; however, there may be less precision in identifying the time of a puncture.

The following table shows the first interrogation in which each new puncture was recorded and the elapsed time since the last previous interrogation. The maximum uncertainty in the time of occurrence of a puncture is 39 hours and 7 minutes.

Table V

Pass	Greenwich date	Greenwich mean time at interrogation	Time since last interrogation, hr	min	Accumulated punctures for detector thickness of - 0.001 in.	0.002 in.
13	Nov. 7, 1964	9:24	3	19	0	1
46	Nov. 9, 1964	17:02	4	7	0	2
84	Nov. 12, 1964	6:50	3	10	0	3
170	Nov. 18, 1964	4:59	6	45	1	4
235	Nov. 22, 1964	17:16	7	14	1	5
308	Nov. 27, 1964	18:06	1	49	1	6
314	Nov. 28, 1964	2:55	3	20	2	7
344	Nov. 30, 1964	4:37	1	45	3	7
354	Nov. 30, 1964	20:56	3	46	4	7
372	Dec. 2, 1964	2:54	17	16	4	8
386	Dec. 3, 1964	2:01	8	25	5	8
409	Dec. 4, 1964	16:29	13	36	6	8
454	Dec. 7, 1964	18:21	26	35	6	9
466	Dec. 8, 1964	13:59	9	36	7	9
485	Dec. 9, 1964	21:27	21	22	8	9
531	Dec. 13, 1964	01:57	12	3	9	9
544	Dec. 13, 1964	23:12	10	11	9	10
558	Dec. 14, 1964	22:13	9	17	10	11
603	Dec. 18, 1964	01:02	26	45	11	11
618	Dec. 19, 1964	1:57	13	54	11	12
640	Dec. 20, 1964	13:34	16	13	12	12
660	Dec. 21, 1964	23:11	7	17	13	12
673	Dec. 22, 1964	20:19	6	48	13	13
739	Dec. 27, 1964	9:15	21	33	14	13
789	Dec. 30, 1964	20:07	6	56	14	14
799	Dec. 31, 1964	12:19	23	8	14	15
812	Jan. 1, 1965	9:43	12	21	15	15
857	Jan. 4, 1965	12:23	5	2	15	16
869	Jan. 5, 1965	7:53	19	30	15	17
880	Jan. 6, 1965	3:23	19	30	15	18
967	Jan 12, 1965	3:19	8	24	15	19
986	Jan. 13, 1965	9:27	8	22	15	20
1043	Jan. 17, 1965	7:38	29	69	15	21
1118	Jan. 22, 1965	12:07	8	47	16	21
1147	Jan. 24, 1965	12:06	10	31	16	22
1170	Jan. 26, 1965	1:26	37	20	17	22
1190	Jan. 27, 1965	11:11	10	40	18	22
1247	Jan. 31, 1965	9:02	10	21	19	22
1346	Feb. 7, 1965	4:42	10	35	20	23
1370	Feb. 8, 1965	19:55	28	30	21	23
1381	Feb. 9, 1965	15:24	19	29	21	24
1415	Feb. 11, 1965	22:34	19	42	21	25
1430	Feb. 12, 1965	23:25	21	32	22	25
1446	Feb. 14, 1965	1:52	3	20	23	25
1468	Feb. 15, 1965	14:39	39	7	24	25

Figure 14 is a plot showing the history of the 24 punctures in the 0.001-inch detectors and the 25 punctures in the 0.002-inch detectors that occurred during the 108 days of orbit time.

Table VI shows the time-area products and the puncture rates.

Table VI

Material thickness, in.	Number of punctures	Time-area products for 108 days, sq ft-days	Puncture rate, punctures $ft^{-2}day^{-1}$
0.001	24	670	0.036
.002	25	1447	.017

Each time one of the sensors is punctured the area of the experiment is reduced. The reduced area is then used until the next puncture occurs. The total time-area product for the 0.001-inch-thick stainless-steel sensors was 670 square foot-days, and the average puncture rate was 0.036 puncture $ft^{-2}day^{-1}$. This average rate is only slightly higher than the puncture rate of 0.031 puncture $ft^{-2}day^{-1}$ which was obtained in 0.001-inch beryllium-copper on the Explorer XVI. (See ref. 4.) The total time-area product for the 0.002-inch sensors was 1447 sq ft-days, and the puncture rate was 0.017 puncture $ft^{-2}day^{-1}$. This average rate is also only slightly higher than the puncture rate of 0.016 puncture $ft^{-2}day^{-1}$ which was obtained in the 0.002-inch beryllium-copper on the Explorer XVI.

Figure 15 shows three curves of predicted puncture rate as a function of thickness for stainless-steel sheet and also shows puncture rates obtained from Explorer XVI and Explorer XXIII. The three curves shown in figure 15 labeled "optimistic," "best estimate," and "pessimistic" have been obtained by using the approach taken by Whipple. (See ref. 5.) In this reference, Whipple derived a "best estimate" formula for the near-earth flux of meteoroids that can penetrate an aluminum sheet as a function of thickness:

$$\log N = -4.02 \log P - 13.33 \qquad (1)$$

where N is the meteoroid flux rate in meteoroids $m^{-2}sec^{-1}$ and P is the thickness in centimeters of type 2024 aluminum sheet.

For making the comparison with the experimentally obtained data, two changes were made to Whipple's formula. The formula was adjusted for earth shielding and was also modified to give the penetration rate in half-hard 302 stainless steel instead of in aluminum.

Whipple assumed that because of earth shielding, the meteoroid flux at a point near the earth would be one-half that existing in free space. Equation (1) corresponds to such a reduced flux. For the mean altitude of Explorer XVI and Explorer XXIII the earth is estimated to shield only about

one-fourth of the 4π steradian influx of micrometeoroids. Therefore, at such an altitude the flux is 3/2 as much as that indicated by equation (1). The flux rate in Whipple's formula (1) has accordingly been multiplied by 3/2 to provide a direct comparison with experimental data.

In the derivation of his formula, Whipple utilized, from Herrmann and Jones (ref. 6), the following equation for the penetration of a semi-infinite target by spherical particles:

$$\frac{p}{m^{1/3}} = 0.6\left(\frac{6\rho}{\pi\rho_t^2}\right)^{1/3} \log_e\left(1 + \frac{K_0^{2/3}B}{4}\right) \tag{2}$$

where

p depth of penetration

ρ projectile density

ρ_t target density

$K_0 = \frac{\rho}{\rho_t}$

$B = \frac{\rho_t v^2}{H}$

H Brinell hardness

v velocity of projectile

In addition, Whipple adopted the relation

$$\frac{P}{p} = 1.5 \tag{3}$$

for the conversion from semi-infinite targets to thin sheets (where P is the thickness of the sheet and p is the depth of penetration). For meteoroids, he adopted the values of $\rho = 0.44$ gram cm^{-3} and $v = 22$ km sec^{-1}. For the type 302 stainless-steel test material used on Explorer XXIII, the density $\rho_t = 7.86$ gm cm^{-3} and the Brinell hardness $H = 2.85 \times 10^{10}$ dynes cm^{-2} have been used. Thus the equation for the rate of penetration of type 302 stainless-steel sheet by meteoroids at an altitude where the earth shields one-fourth of the total flux is given by

$$\log N = -4.02 \log P - 14.61 \tag{4}$$

or, with N defined as micrometeoroids $ft^{-2}day^{-1}$ and P defined as sheet thickness in inches, the equation becomes

$$\log N = -4.02 \log P - 12.33 \quad (5)$$

By the same procedure Whipple's "pessimistic" and "optimistic" formulas, respectively, become

$$\log N = -4.02 \log P - 11.12 \quad (6)$$

$$\log N = -3 \log P - 11.16 \quad (7)$$

Equations (5), (6), and (7) are represented in figure 15.

Experimental results obtained in the hypervelocity impact laboratory at the Langley Research Center indicate that the penetration depths in beryllium-copper targets and in steel targets are about the same when obtained under similar impact conditions. (See refs. 1 and 7.) This equivalence is also confirmed by using the Herrmann and Jones equation (2) to compute the penetration in beryllium-copper with a density of 8.26 gm cm^{-3} and a Brinell hardness H of 1.0×10^{10} dynes cm^{-2}. The Explorer XVI data for the 0.001-inch and the 0.002-inch-thick beryllium-copper have also been plotted in figure 15. The width of the bar extending through each point of the Explorer XVI and Explorer XXIII data corresponds to the variation in thickness of the test material.

Confidence limits (confidence coefficient, 0.95) for the Explorer XVI and Explorer XXIII data points plotted in figure 15 have been indicated in the figure. These limits were computed by using the chi-square distribution in the manner described in reference 4. The limits on the Explorer XXIII data indicate that one can expect with 95-percent confidence that the puncture rate in puncture $ft^{-2}day^{-1}$ will lie between 0.023 and 0.053 for 0.001-inch stainless steel, and between 0.011 and 0.025 for 0.002-inch stainless steel.

In figure 15, the puncture rates obtained from stainless steel on Explorer XXIII are close to the puncture rates obtained from beryllium-copper on Explorer XVI. The confidence limits easily include the data points obtained from Explorer XVI. These data fall between the "best estimate" and "optimistic estimate" curves in figure 15. Explorer XXIII data as well as the Explorer XVI data, however, indicate a more gradual decrease of puncture rate with increasing skin thickness for this range of thickness than is shown by the curves.

Figure 15, which shows penetration data and estimates for stainless-steel and beryllium-copper sheet, has been replotted, in simplified form, for aluminum sheet in figures 16 and 17. Figure 16 is for the case in which the earth shields half of the meteoroid flux; figure 17 is for the case of no shielding. The solid line in figure 16 is the plot of Whipple's best estimate given by equation (1) with the constant 13.33 replaced by 11.05 because of the change of units. The solid line in figure 17 is the same as that of figure 16 except for the factor of 2. The dashed lines in figures 16 and 17 were obtained by converting the observed penetration frequencies for beryllium-copper and stainless steel (Explorers XVI and XXIII) to penetration frequencies for aluminum sheet by means of the Herrmann and Jones penetration equation.

Meteoroid Impact Detection System

The meteoroid-impact detection system appears to be functioning in all three sensitivity ranges. However, only the impact counts recorded on the high-sensitivity system are presented for this reporting period.

The high-sensitivity system (0.03 dyne-sec) has accumulated a total of 274 counts for the period from orbital injection to the 44th day in orbit. The accumulated impact count per day for this range is shown in figure 18. The data presented in the figure represent only 218 of the total counts recorded, because sufficient data are not yet available past the 34th day in orbit to resolve total counts to counts per day.

The vertical dashed lines shown for the 3d, 5th, and 7th days in orbit in figure 18 indicate the number of counts registered during a 1-minute data transmission taken from one of the 14 daily scheduled interrogations. These 1-minute count rates, which are much higher than the average rate for the reporting period, have not been found to occur in any of the other interrogation records analyzed through the 34th day in orbit. No peculiarity of the telemeter system is known that can cause a high counting rate during an interrogation; however, the matter is still under study.

The counts measured during the first few days in orbit show the same general trend as was obtained from Explorer XVI; that is, the count rates are high for the first few days in orbit and then decrease to a lower level. The count rates appear to be somewhat lower than those obtained from the most sensitive system (0.5 dyne-sec) on Explorer XVI.

Capacitor Detector

No discharges of either detector have been recorded during the 44 days from launch to December 19, 1964. The capacitor-detector monitoring circuits indicate that both detectors have bias voltage.

It is estimated that Explorer XXIII is exposed to an omnidirectional flux of 10^{10} to 10^{11} electrons/cm^2-day in the energy range 0.5 to 8.0 MeV. Based on this rate the electron dose in this energy range for the 44-day period would be of the order of 10^{11} to 10^{12} electrons/cm^2. There is little information available concerning the flux rate in space for the energy spectrum from about 50 keV to 0.5 MeV. It is generally considered to represent 95 percent of the total flux rate from 50 keV to 8.0 MeV. The corresponding omnidirectional electron dose rate for energies from about 50 keV to 8.0 MeV would then be about 10^{11} to 10^{12} electrons/cm^2-day, and the total dose would be about 10^{12} to 10^{13} for the 44 days in orbit.

For correlation of Explorer XXIII results with the results of ground tests, these doses should be reduced by about an order of magnitude in order to take into account the facts that (1) the sensor face is shielded from half the omnidirectional flux, and (2) the electrons in space are incident at all angles,

whereas in the laboratory studies the electron irradiation was normal to the surface. The effective dose is thus considered to be about 10^{11} to 10^{12} electrons/cm^2.

The equivalent dose rate to each sensor, based on the preceding calculations, is from 10^{10} to 10^{11} electrons/cm^2-day. In the radiation ground tests, discussed in the appendix, the sensor received a total dose of 10^{13} electrons-cm^{-2}. The sensors on the Explorer XXIII will have to be exposed to the space environment for 100 to 1000 days to receive a dose equivalent to that in the ground tests. This range of uncertainty precludes any attempt to predict accurately when radiation-induced pulsing might be expected. However, it does appear that if the same number of pulses occurs in flight as occurred in the ground tests, their frequency of occurrence would be low because of the relatively long flight time required to achieve an equivalent dose.

Cadmium Sulfide Cells

The cadmium sulfide cell detectors are the same type as those flown successfully on Explorer XVI. The detectors on Explorer XXIII were functioning properly during all interrogations made prior to lift-off but on the first interrogation made shortly after fourth-stage burnout they were saturated with light. Apparently, the aluminized PET film covers were damaged during the launch, and thus the detectors could not provide meteoroid-penetration data.

Test Solar Cells

During the period covered by the report, no degradation of the solar cells due to radiation has been observed. Based on the best available radiation-flux estimates for this orbit, little, if any, damage was expected.

Telemetry Performance

Telemetry data taken before and after launch indicate that the telemetry system performance after injection into orbit was satisfactory and that all sensors except the cadmium sulfide sensors were operating. Telemetry data recorded by Antigua, BWI, just after injection into orbit at 12 hours 11 minutes 37 seconds GMT (T + 9 minutes, 36 seconds) indicate that both cadmium sulfide sensors were saturated with light.

A total of 324 data interrogations from launch to the 44th day in orbit, December 19, 1964, have been automatically processed at Langley Research Center. Of these, 296 data listings from telemeter A were usable and 262 data listings from telemeter B were usable. In general, the data interrogations not processable were noisy and the data, if they were needed, could be recovered by manual analysis. However, because of the inherent data-storage capability and the slow data rates of the primary experiments, the data can always be recovered during subsequent interrogations. Manual analysis of the data has not yet been required.

Data listings analyzed through the 44th day in orbit indicate that the telemetry performance is still satisfactory. Up to the 25th day in orbit, November 30, 1964, sufficient data are available to define the upper and lower temperature and voltage limits for the telemetry system for each day; beyond the 25th day processed data are still sparse. Figure 19 is a plot of the telemeter temperature. These temperatures have remained within the calibration limits, -10° C to 50° C, of the telemeter system and roughly parallel the curve of the percentage time in sunlight (fig. 20). Figures 21 and 22 are plots of the telemeter nickel-cadmium battery voltage and battery module temperature. These temperatures also parallel the curve of percentage time in sunlight. The decrease in battery voltage with increasing battery temperature is normal. The battery module temperature has remained within acceptable limits and the battery voltages are normal.

A special station was set up at Antigua, BWI, to interrogate and record data at insertion in order to establish a zero reference for all sensors. From received-signal-strength records made at Antigua, BWI, it has been determined that spinup of the Scout fourth stage occurred at 12 hours, 10 minutes, 45.8 ± 1 second GMT and the spin rate was 144 ± 1 rpm. Spin rate after fourth-stage burnout was 150 ± 1 rpm.

Received-signal-strength records from the Station Tracking and Data Acquisition Network (STADAN) stations indicate signal strength from -88 dBm to -120 dBm with most of the recordings from -90 dBm to -100 dBm (where dBm is the decibel power ratio in which the reference power is 1 milliwatt). Automatic data analysis requires a signal strength greater than -110 dBm. These received-signal-strength records were also examined to determine spin and coning rates by using the antenna nulls. These spin rates are summarized and presented in another section.

The radio beacon used to facilitate tracking was designed to operate for a minimum of 7 days. Reports from the STADAN station indicated that the beacon was still usable but very weak on the twelfth day after launch, November 18, 1964. Johannesburg, Republic of South Africa, reported that there was no beacon at 1213 GMT on November 20, 1964.

During the first 5 days in orbit reports from STADAN indicate that data transmission occurred from Explorer XXIII on four occasions without known ground commands from STADAN stations. These occasional extra transmissions are not expected to affect the operation of the power system, since there is an automatic turnoff system built into the satellite.

Thermal Control System

Like the thermal control in all previous S-55 series payloads, the thermal control is entirely passive. Since the Explorer XXIII is built around the last-stage motor of the Scout (X-258-C1) and does not separate from that stage, it was necessary to provide protection for the spacecraft from the hot motor case just after burnout as well as to provide for maintenance of temperatures within acceptable limits while in orbit. A flight test of a X-258-C1 rocket motor,

using the Javelin launch vehicle, has shown that motor-case temperatures as high as 440° C may be encountered shortly after burnout. In that test the rocket motor was radiating directly to space and the peak temperature was reached about 8 minutes after burnout. To reduce heat transfer from the hot motor case to the Explorer XXIII payload, a layer of aluminum foil was bonded to the motor case and a multilayer blanket of aluminum foil was placed between the motor case and the payload. Motor-case temperatures were expected to reach about 540° C on the side wall and about 425° C on the dome.

Figures 23 and 24 show calculated temperatures, after burnout, for the telemeter canisters and battery modules for a peak temperature of 425° C on the forward dome of the motor. The actual temperatures recorded by thermistors encapsulated in these structures are also shown in figures 23 and 24; they are about 10° C below the calculated values.

Figures 25 and 26 show the calculated temperature histories for the fourth and sixth rows of pressure cells for peak temperatures of 540° C and 650° C on the cylindrical section of the motor case. On both rows the highest recorded pressure cell temperatures fall between the two curves and closer to the higher one. The recorded temperature dropped off faster than predicted, but this drop-off is at least partly due to assuming that the motor radiated only to the payload and thus neglecting loss of heat by radiation through the nozzle.

Figures 27 to 30 show temperatures recorded from November 6, 1964, to November 27, 1964, by thermistors inside the telemeter canisters and battery boxes and also for the pressure cells and capacitor detector panels. The two horizontal lines on each figure represent the highest and lowest temperatures expected around the orbit after the motor case heat is dissipated during the first 2 weeks. (These maxima and minima should change little during the first 2 weeks in orbit.) The minimum temperatures recorded are shown in table VII. Predicted values are shown for comparison. The minima occurred during the last few days of November 1964.

Table VII

	Minimum temperature, °C		Maximum temperature, °C	
	Predicted	Observed	Predicted	Observed
Telemeter modules	-4	0	36	37
Battery boxes	-11	-4	36	37
Pressure cells	-33	-27	43	32
Capacitor detectors	-30	-25	44	30

This period was the period of lowest satellite temperatures for the following reasons: First, the angle between the satellite axis and the sun was small - about 25° at injection. Secondly, the percent time in sunlight was low,

and varied between 65 and 68 percent during the period shown. This time increased to 100 percent about 40 days after launch, as shown in figure 20. Third, the transition from spin about the satellite longitudinal axis to tumble about a transverse axis (for which a much larger area would be presented to the sun) was far from complete as shown in a previous section. The maximum temperatures, recorded during the period of 100-percent sunlit orbits from December 17 to December 25, are also shown in table VII. The maxima are well within operating limits and agree well with predictions.

In summary, pressure-cell temperature data measured on the satellite during the first several passes show good correlation with those calculated by using Javelin flight temperature data. No damage to the payload resulted from this initial heating from the rocket case. Data presented show that, after dissipation of this heat, the payload temperatures are about as expected through November 27, 1964. Although telemeter and battery temperatures were somewhat low, they were acceptable for proper operation and increased as the coning angle of the satellite continued to increase and as the percent time in sunlight increased. Maximum temperatures during the period of 100-percent sunlight were at or below predicted maxima.

CONCLUSIONS

From the data obtained during this reporting period, it appears that both the primary and secondary objectives of the Explorer XXIII spacecraft are being successfully fulfilled. The orbit achieved was close to that predicted prior to launch. Data presented in this report indicate:

1. The puncture rate in 0.002-inch stainless steel, derived on the basis of 25 punctures received to date, is 0.017 $ft^{-2}day^{-1}$. With 95-percent confidence, the average puncture rate in 0.002-inch stainless steel lies between 0.011 and 0.025 puncture $ft^{-2}day^{-1}$.

2. The puncture rate in 0.001-inch stainless steel, derived on the basis of 24 punctures received to date, is 0.036 $ft^{-2}day^{-1}$. With 95-percent confidence, the average puncture rate in 0.001-inch stainless steel lies between 0.023 and 0.053 puncture $ft^{-2}day^{-1}$.

3. The puncture rates obtained for stainless steel on Explorer XXIII are close to the puncture rates obtained for beryllium-copper on Explorer XVI. The confidence limits easily include the data points obtained from Explorer XVI.

4. There were no counts recorded by the capacitor-detector experiment through December 19, 1964. The capacitor-detector monitoring circuit indicates that both detectors have bias voltage.

5. All components of the solar-cell radiation experiment are functioning properly. No measurable degradation of the test cells has been observed through December 19, 1964.

6. The meteoroid-impact detection system has been operating. Counting rates on the high-sensitivity system have averaged lower than the rates indicated by a less sensitive system on the Explorer XVI.

7. Both of the cadmium sulfide cell meteoroid-penetration experiments were found to be inoperative immediately after launch. Presumably, the aluminized poly [ethylene terephthalate] film covers were damaged during spacecraft launch.

8. Telemeter performance was satisfactory throughout this reporting period.

9. The temperatures of all systems have remained within acceptable limits.

Langley Research Center,
National Aeronautics and Space Administration,
Langley Station, Hampton, Va., June 3, 1965.

APPENDIX

CAPACITOR-TYPE METEOROID-PENETRATION DETECTOR DEVELOPMENT

The development of a capacitor type of meteoroid-penetration detector at the Langley Research Center has included an extensive environmental test program. These tests have included electron irradiation, temperature cycling in vacuum, vibration, and particle impact. Radiation tests, conducted in an electron radiation facility, indicated sporadic pulsing of the detector, apparently because of electron storage in the dielectric with subsequent discharge to one of the detector electrodes. The wave form of some of the spurious pulses has been found to be similar to that of a meteoroid penetration discharge. The capacitor detector is being flown on Explorer XXIII to collect data on the effects of the space electron radiation environment on the detector, in particular, to determine whether the energetic electrons in space might similarly collect in the dielectric and produce spurious counts when they discharge.

The exposed area of the detectors was kept small (0.782 ft^2) to reduce the probability of meteoroid penetrations, and thus better define the origin of any observed large numbers of discharges as being radiation induced. The predicted meteoroid-penetration rate in the detectors is approximately 1 hit per month based on Explorer XVI data. If the number of pulses is near one per month, it will be difficult to establish confidently the cause of the pulses.

A sensor configuration of the type flown on Explorer XXIII was irradiated in the materials radiation laboratory at the Langley Research Center to determine its performance in the radiation environment. The tests were conducted at room temperature (approximately 25° C) with a dose rate of 10^{10} electrons/cm^2-sec. A total of 10 runs were made on the sensor, each at a different electron energy level, to cover, in increments of 100 keV, the energy range from 100 keV to 1000 keV. In each run the sensor received a total dose of 10^{13} electrons-cm^{-2}. The minimum number of pulses observed in any run was zero and the maximum number observed in any one run was 6. A total of 20 pulses was observed for the 10 runs.

Capacitor-Detector Fabrication

The configuration of the thin film capacitor is shown by figures 6 and 7. The penetration material consists of 0.001-inch-thick, type 302 stainless steel in the half-hard condition. The stainless-steel penetration material also serves as one electrode of the capacitor. The dielectric material consists of a bilaminate of two sheets of 0.15-mil poly[ethylene terephthalate] film (PET) laminated to each other and to the stainless steel with 30 microinches of an adhesive. The total thickness of the bilaminate dielectric is approximately 0.28 mil instead of the presumed 0.36 mil (0.15 + 0.15 + 0.03 + 0.03), because of stretching of the polymer film during lamination. Approximately 12 microinches of copper is vacuum deposited to the outer layer of the dielectric to serve as the second electrode.

The bilaminate dielectric system was found to be more satisfactory than a single layer of 0.25-mil PET film. The reason is that pinholes in a single sheet may fill with copper and cause an electrical short when the copper electrode is deposited, whereas the probability that such imperfections would be superimposed in a bilaminate is negligible. The use of two layers of 0.15-mil film greatly reduces the number of electrical shorts occurring during fabrication.

A silicon monoxide thermal balance coating was applied to the outer surface of the stainless-steel foil. The coating is the same as that used on the pressurized cells.

An electrical connection to the vacuum-deposited copper surface was made by soldering a 1.0-mil copper ribbon directly to the surface. The soldering was accomplished by using a 63-37 solder, a standard flux, and a controlled temperature (205° C) soldering iron. No failures of soldered connections were observed in any of the environmental tests.

The capacitor was mounted on a 1/4-inch-thick layer of polyurethane foam support by using a 0.10-mil-thick adhesive. The foam acts both as a low-density support structure and an absorber for the spray resulting from a meteoroid penetration. A laminated fiber-glass tray was used as the mounting fixture. A printed circuit was laminated to the rear surface of the fiber-glass tray as a means of bringing the capacitor leads to terminal pins.

A thermistor temperature-sensing element is located on the rear face of a 3/4 inch by 1/4 inch sample cross section of the detector. Figure 6 shows the location of the thermistor on the detector panel.

A total of 10 detector units were fabricated from the same material batches in order to keep the units as nearly identical as possible. Six of the 10 units were designated as test units and used for the environmental tests. These tests consisted of temperature cycling in vacuum, electron irradiation, and vibration. Additional test samples were fabricated for the impact tests. Two of the 10 detectors were designated as flight units and the other two detectors were used as flight backup units.

Capacitor-Detector Circuit

Capacitor.- The copper electrodes of the two detectors on the Explorer XXIII spacecraft are charged to a nominal potential of -13 V dc through the signal conditioning circuits. The stainless-steel electrodes are at ground potential. Each of the two capacitor-detector units is wired into a separate signal conditioner unit and to a separate telemeter. The actual voltages can vary slightly, depending on the power-supply battery voltage. An electrical discharge of the capacitor in excess of 2 volts is accepted by the signal conditioner unit and stored in a counter to be telemetered to a ground station upon interrogation.

APPENDIX

Signal conditioner unit.- The signal conditioner circuit was designed to bias the capacitor detector with a -13 V dc potential and produce a uniform output signal to the counter when triggered by a fast rise time discharge of the capacitor. A block diagram of the detector circuitry is shown in figure 31. Each signal conditioner unit has been calibrated to determine its triggering characteristics as shown in figure 32. The calibration curves show the pulse amplitude and duration that is required to trigger the signal conditioning unit. Any combination of pulse amplitude and duration falling above the curve will trigger the unit, whereas any combination of pulse amplitude and duration falling below the curve will not trigger the unit. These curves were obtained by inducing pulses of various amplitude and duration into the signal conditioning unit and recording the output. A calibration was performed at 20° C and at 0° C.

Detector monitor unit.- Each capacitor detector is supplied with a monitoring circuit as shown in figure 31 to determine the condition of the detector at each interrogation of the satellite. The monitor unit consists of a voltage divider circuit wired to the biased side of the detector. This voltage is fed to a subcarrier oscillator in the telemeter. If the detector should become electrically "open" or "shorted," the monitor unit voltage would drop to zero.

Environmental Testing

Thermal-vacuum tests.- Each of the 10 detectors was vacuum soaked for a minimum of 96 hours at a pressure of 1×10^{-5} mm Hg. During the vacuum soak the detectors were heated and cooled by quartz-tube radiators and liquid nitrogen coils, respectively. Each detector was cycled a minimum of four times. During the testing each detector was charged to a -13 V dc potential through a flight-type signal conditioning circuit. The output of the signal conditioning circuit was monitored with a recording oscilloscope. In addition, some detectors were monitored during each test with a high-frequency response oscilloscope.

Each of the detectors was tested from -80° C to 120° C with continuous electrical measurements made during each thermal cycle. After approximately 48 hours of vacuum soak and 1 to 2 thermal cycles the leakage current through the capacitor became constant. The capacitance of the 10 detectors ranged from 0.111 μf to 0.122 μf measured at 1 kc. The capacitance value for the detector changed approximately 10 percent for the full temperature cycle. No discharging or shorting was observed during the thermal vacuum testing.

Vibration tests.- Some detector units were given vibration tests through the entire vibration spectrum used in payload vibration tests. These tests were designed to determine the structural integrity of the printed wiring, the pin connections, the laminate of PET film and stainless steel, and the assembled unit. In addition, prototype and flight units were vibration tested on their respective payloads. No electrical or mechanical difficulties were observed during these tests.

APPENDIX

The vibration spectrum and levels for these tests are shown in the following table:

Table VIII

Frequency, cps	Amplitude, g	Sweep rate
20 to 2000	1	2 octaves/min
75 to 500	6	2 octaves/min
500 to 2000	12	2 octaves/min
50 to 70	6	2 octaves/min
40 to 70	3 for 24 sec	
Random, 20 to 2000	11.3 root mean square for 4 minutes	

Projectile impact tests.- Projectile impact tests were run on a number of capacitor-detector test samples. The projectiles were accelerated by means of an electrical discharge type of small-particle accelerator. A large capacitor bank discharges through a small lithium rod which vaporizes to a gas at a high temperature and pressure. The gases escape through a nozzle at high velocities and drag accelerate 1-mil borosilicate spheres to velocities ranging from 10,000 ft/sec to 40,000 ft/sec.

Each sample detector was charged to a -15 V dc potential and the discharge resulting from a projectile penetration was monitored on an oscilloscope for signal amplitude and shape. The average signal amplitude with a -15 V dc potential was approximately 3 to 4 volts, with a minimum amplitude of 1.0 volt and a maximum amplitude of 12.0 volts. A typical capacitor discharge from a hypervelocity projectile impact is shown in figure 33. The two oscilloscope traces shown in the figure are for the same discharge but were obtained at different sweep speeds. In the upper sketch, the trace was swept at 100 microseconds per division and in the lower sketch the beam was swept at 1 microsecond per division.

REFERENCES

1. Hastings, Earl C., Jr., compiler: The Explorer XVI Micrometeoroid Satellite - Description and Preliminary Results for the Period December 16, 1962, Through January 13, 1963. NASA TM X-810, 1963.

2. Hastings, Earl C., Jr., compiler: The Explorer XVI Micrometeoroid Satellite - Supplement I, Preliminary Results for the Period January 14, 1963, Through March 2, 1963. NASA TM X-824, 1963.

3. Hastings, Earl C., Jr., compiler: The Explorer XVI Micrometeoroid Satellite - Supplement II, Preliminary Results for the Period March 3, 1963, Through May 26, 1963. NASA TM X-899, 1963.

4. Hastings, Earl C., Jr., compiler: The Explorer XVI Micrometeoroid Satellite - Supplement III, Preliminary Results for the Period May 27, 1963, Through July 22, 1963. NASA TM X-949, 1964.

5. Whipple, Fred L.: On Meteoroids and Penetration. J. Geophys. Res., vol. 68, no. 17, Sept. 1963, pp. 4929-4939.

6. Herrmann, Walter; and Jones, Arfon H.: Correlation of Hypervelocity Impact Data. Proc. of the Fifth Symposium on Hypervelocity Impact, vol. 1, pt. 2, Apr. 1962, pp. 389-438. (Sponsored by U.S. Army, U.S. Air Force, and U.S. Navy.)

7. Collins, Rufus D., Jr.; and Kinard, William H.: The Dependency of Penetration on the Momentum Per Unit Area of the Impacting Projectile and the Resistance of Materials to Penetration. NASA TN D-238, 1960.

Figure 1.- Photograph of Explorer XXIII. L-64-8758

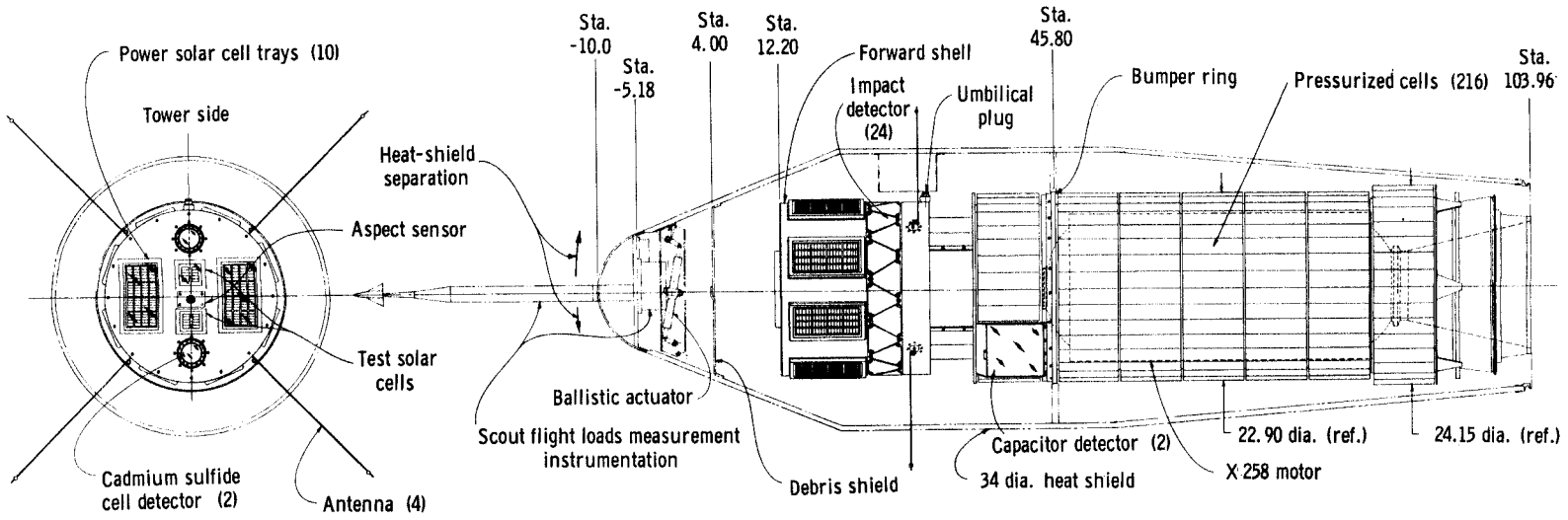

Figure 2.- Payload assembly drawing. All dimensions are in inches.

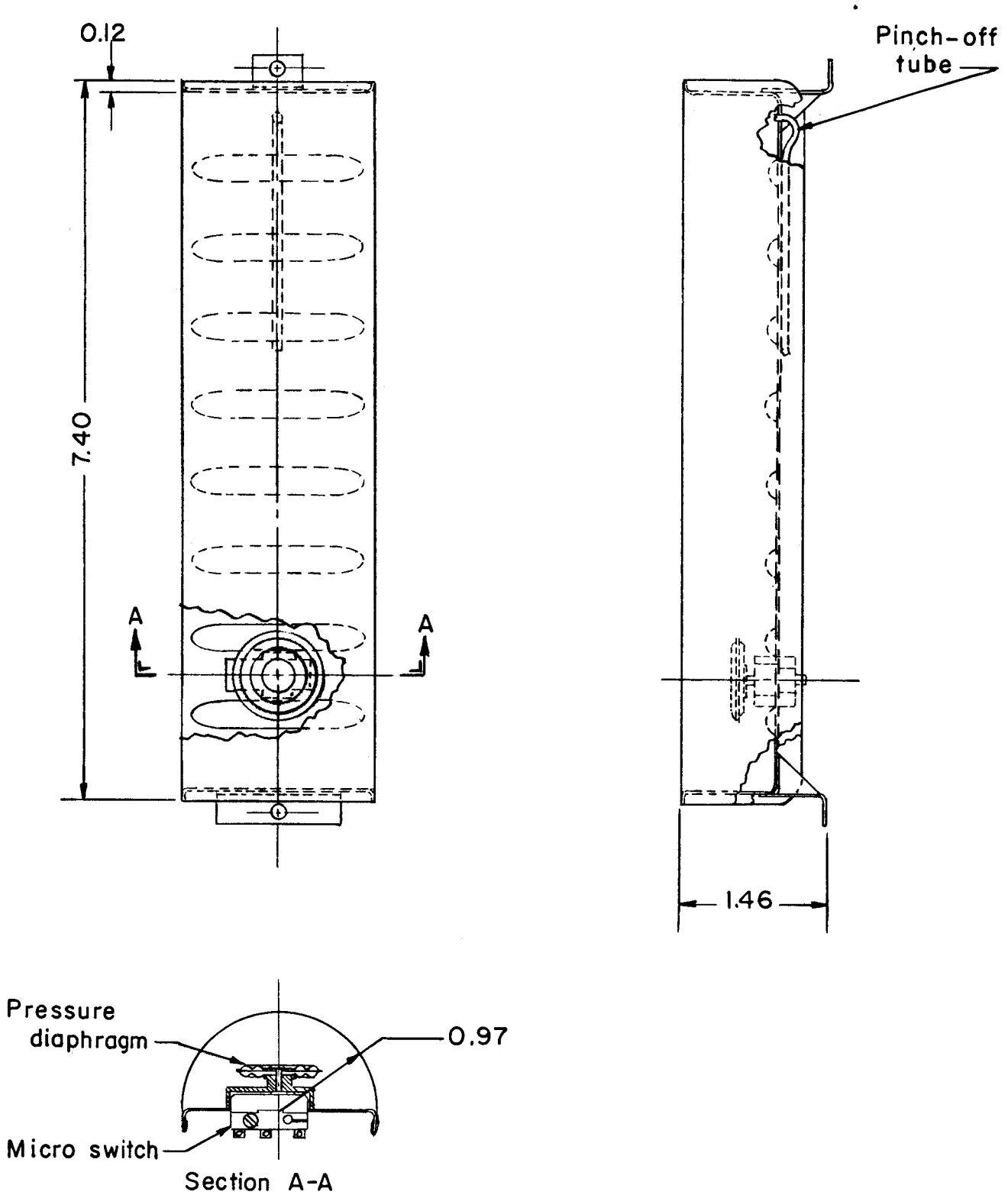

Figure 3.- Pressurized-cell detector. All dimensions are in inches.

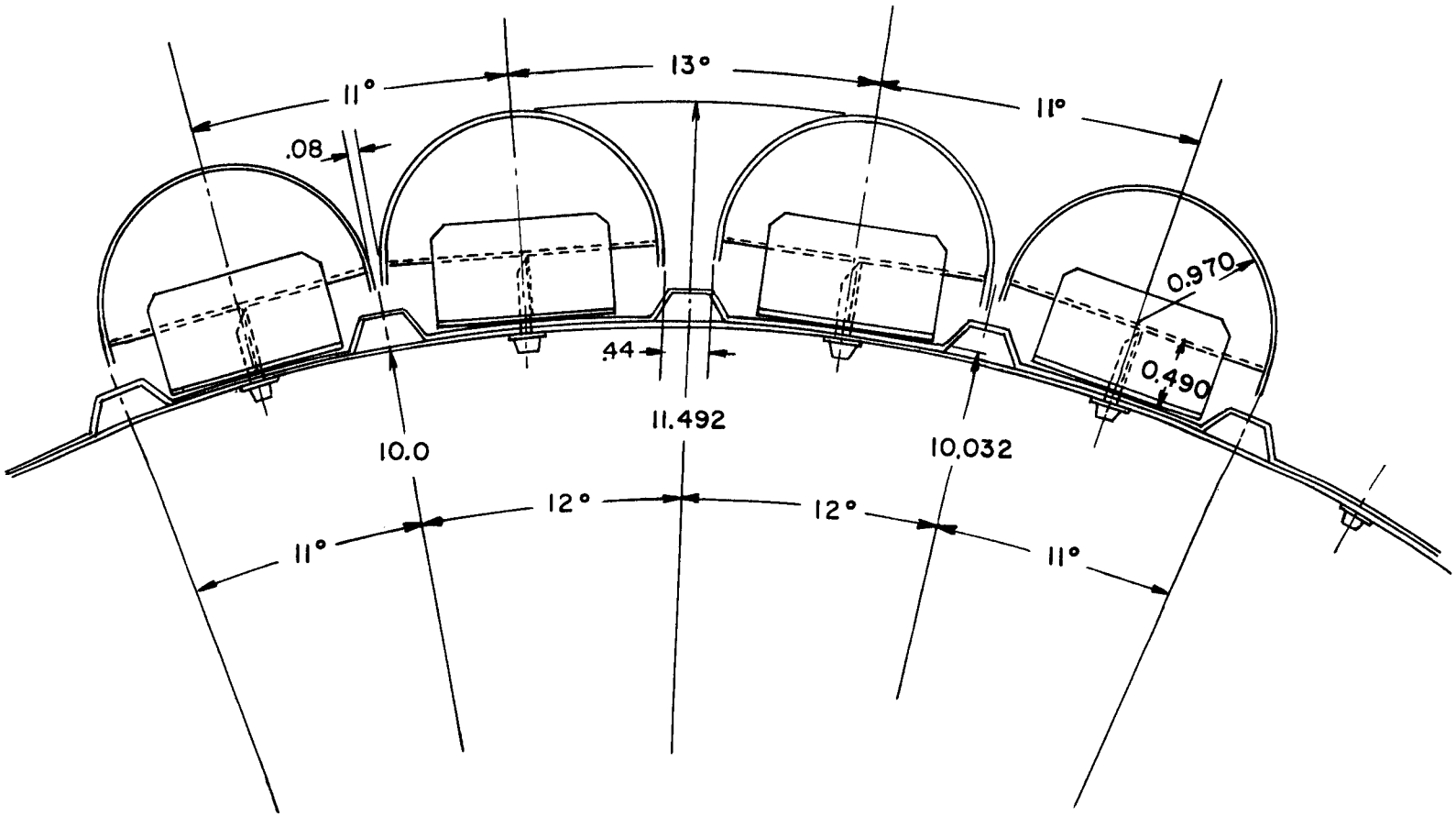

Figure 4.- Mounting arrangement of pressurized cells. All dimensions are in inches.

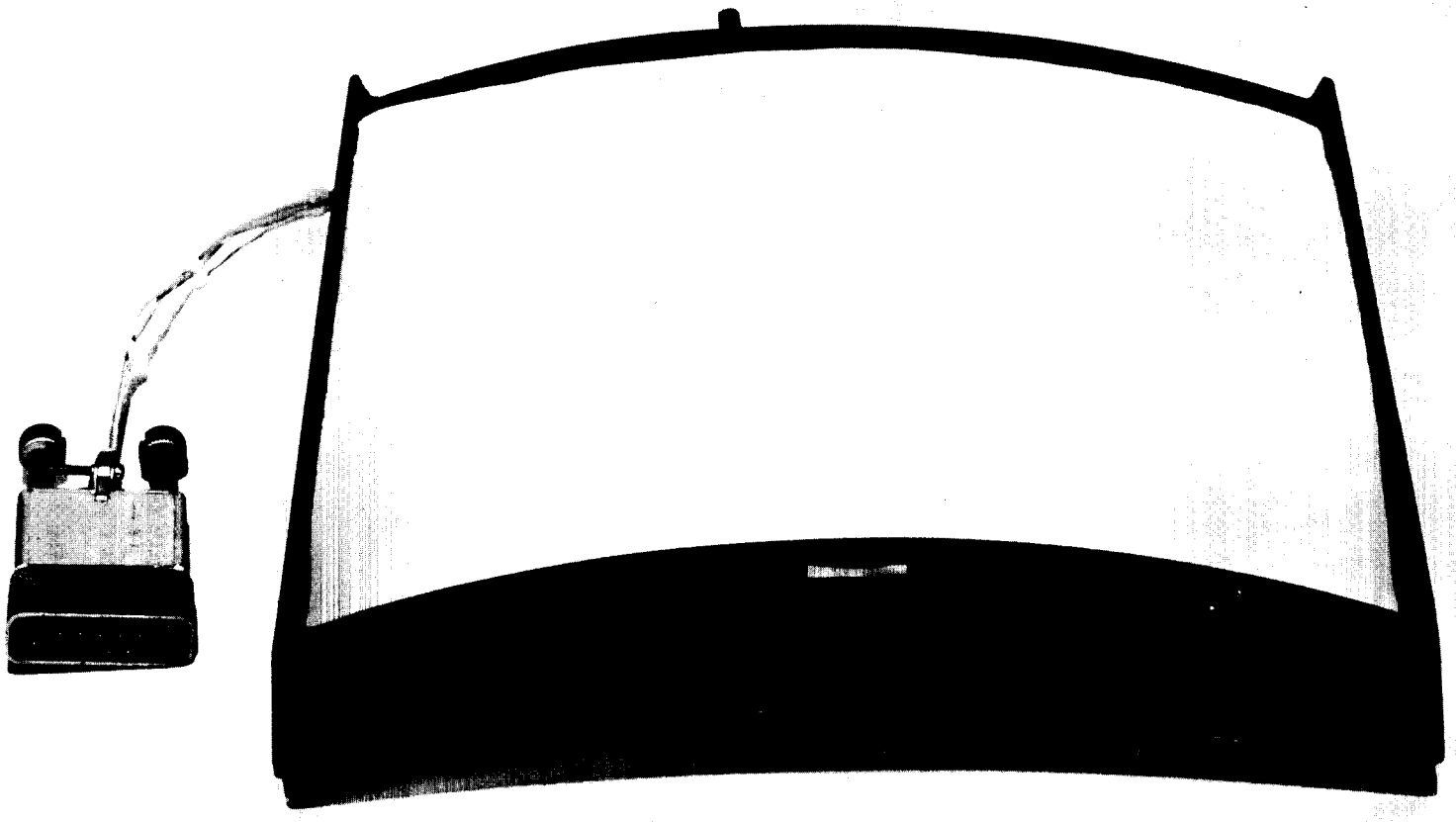

Figure 5.- Photograph of capacitor micrometeoroid detector.

L-64-8916.1

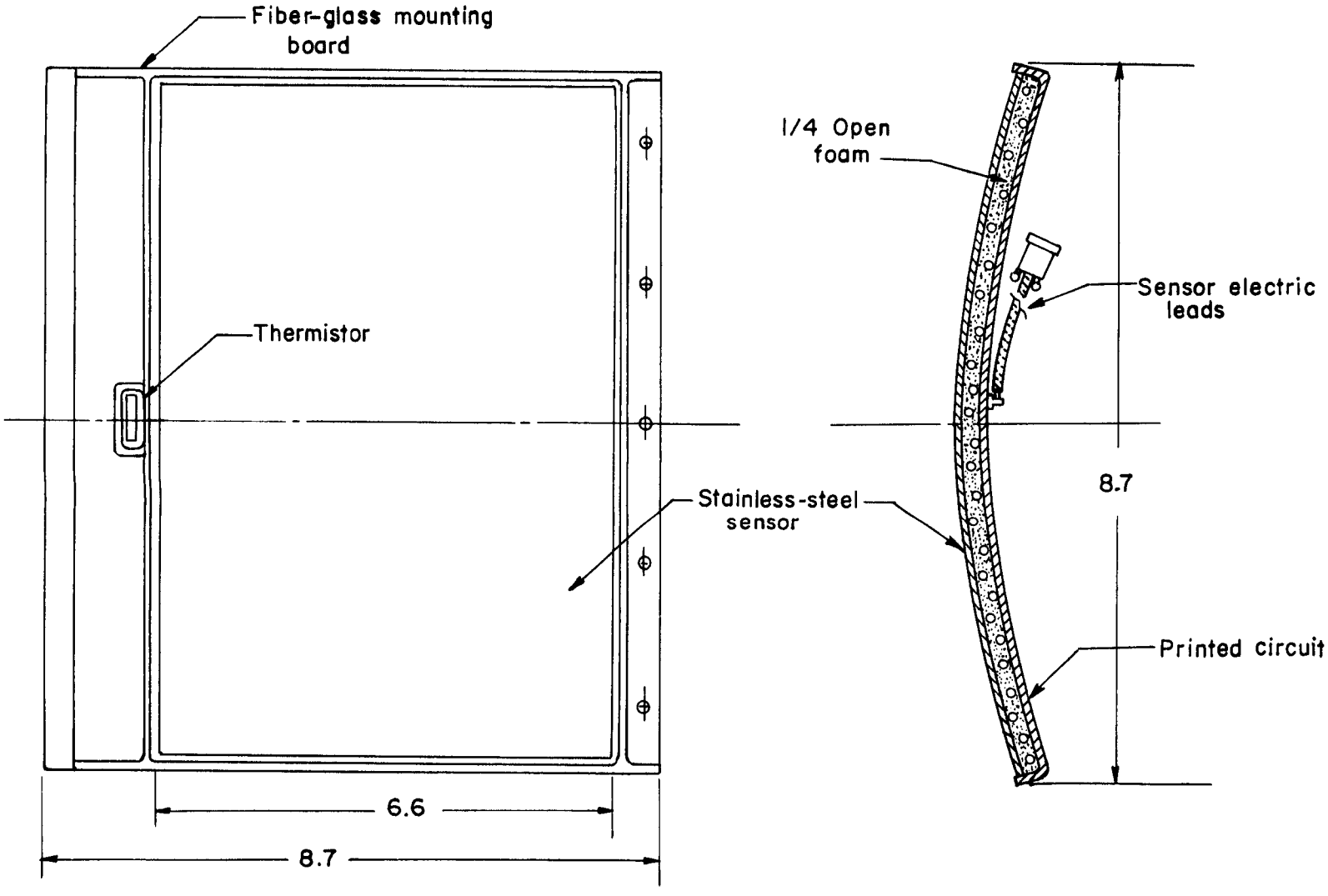

Figure 6.- Capacitor micrometeoroid penetration detector. All dimensions are in inches.

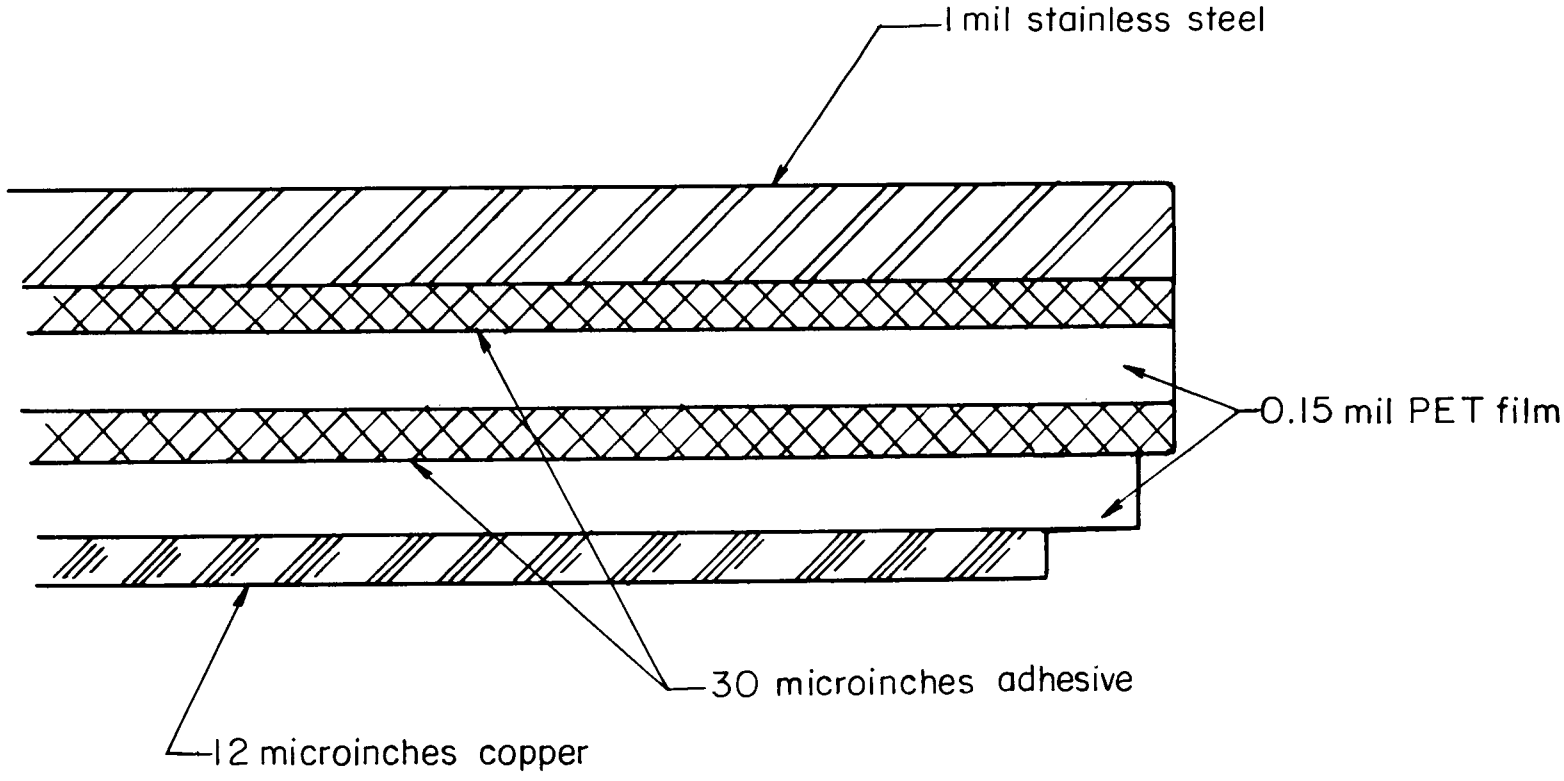

Figure 7.- Typical cross section of capacitor micrometeoroid detector.

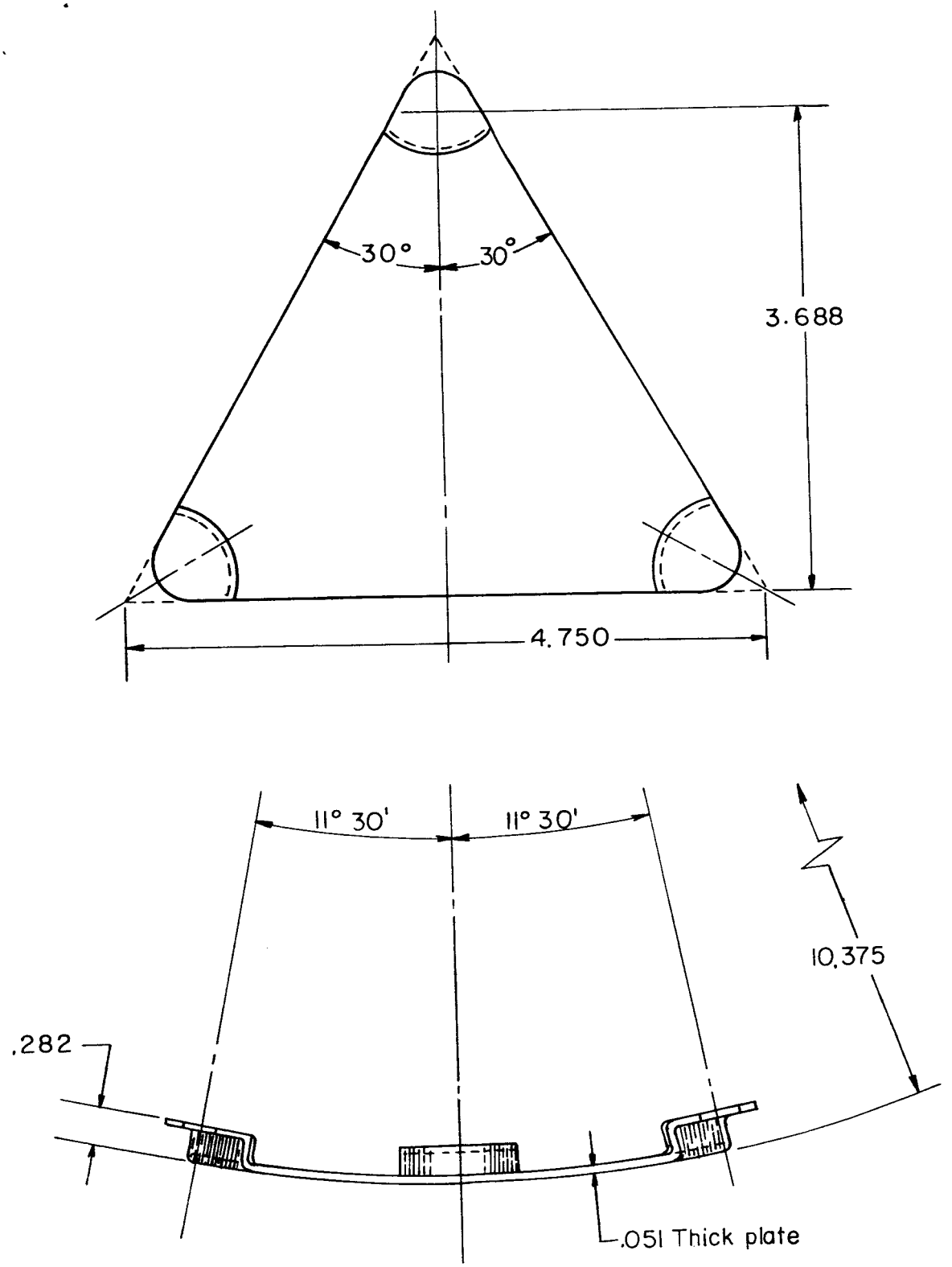

Figure 8.- Impact detector. All dimensions are in inches unless otherwise indicated.

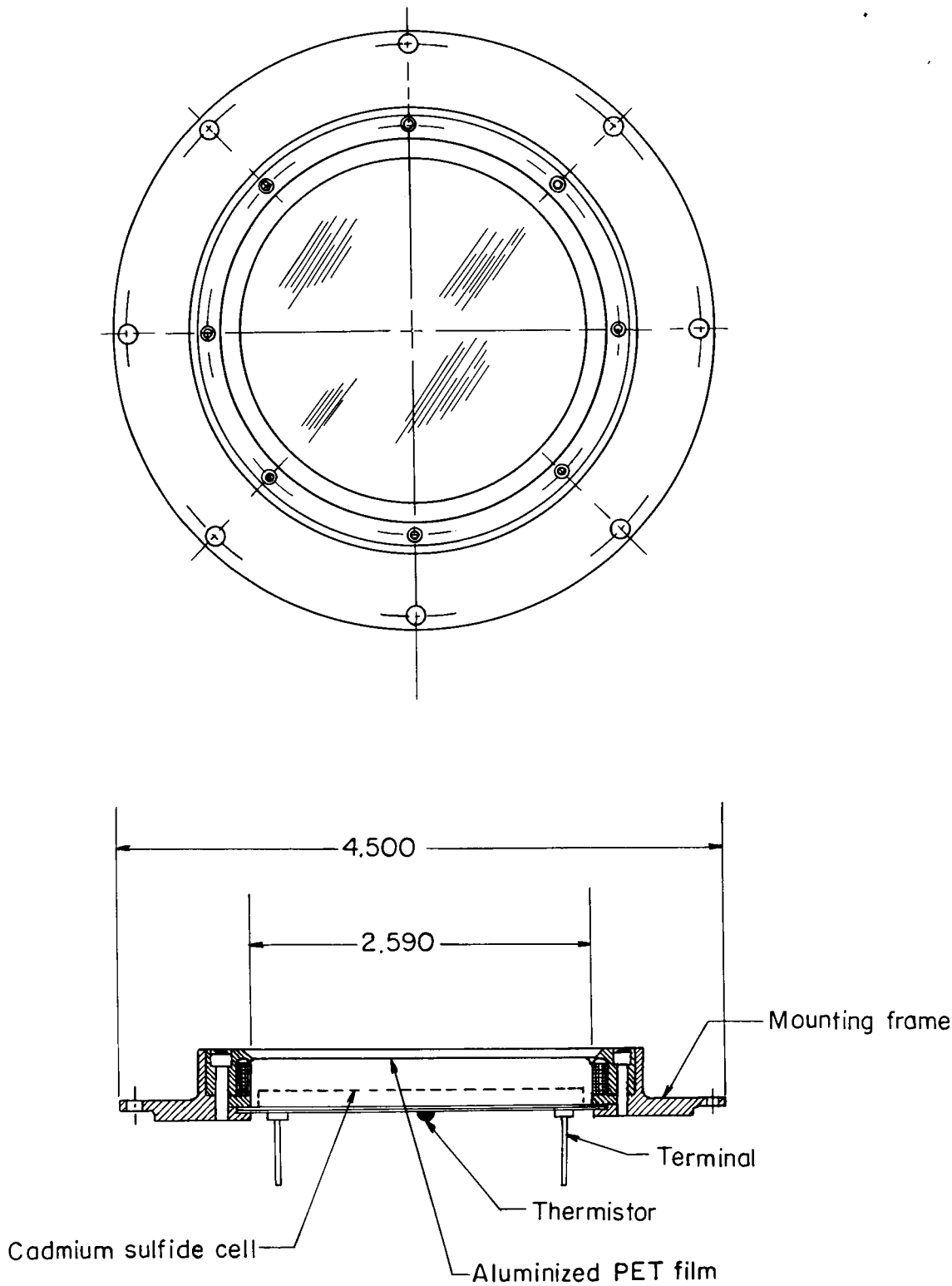

Figure 9.- Sketch of cadmium sulfide detector. All dimensions are in inches.

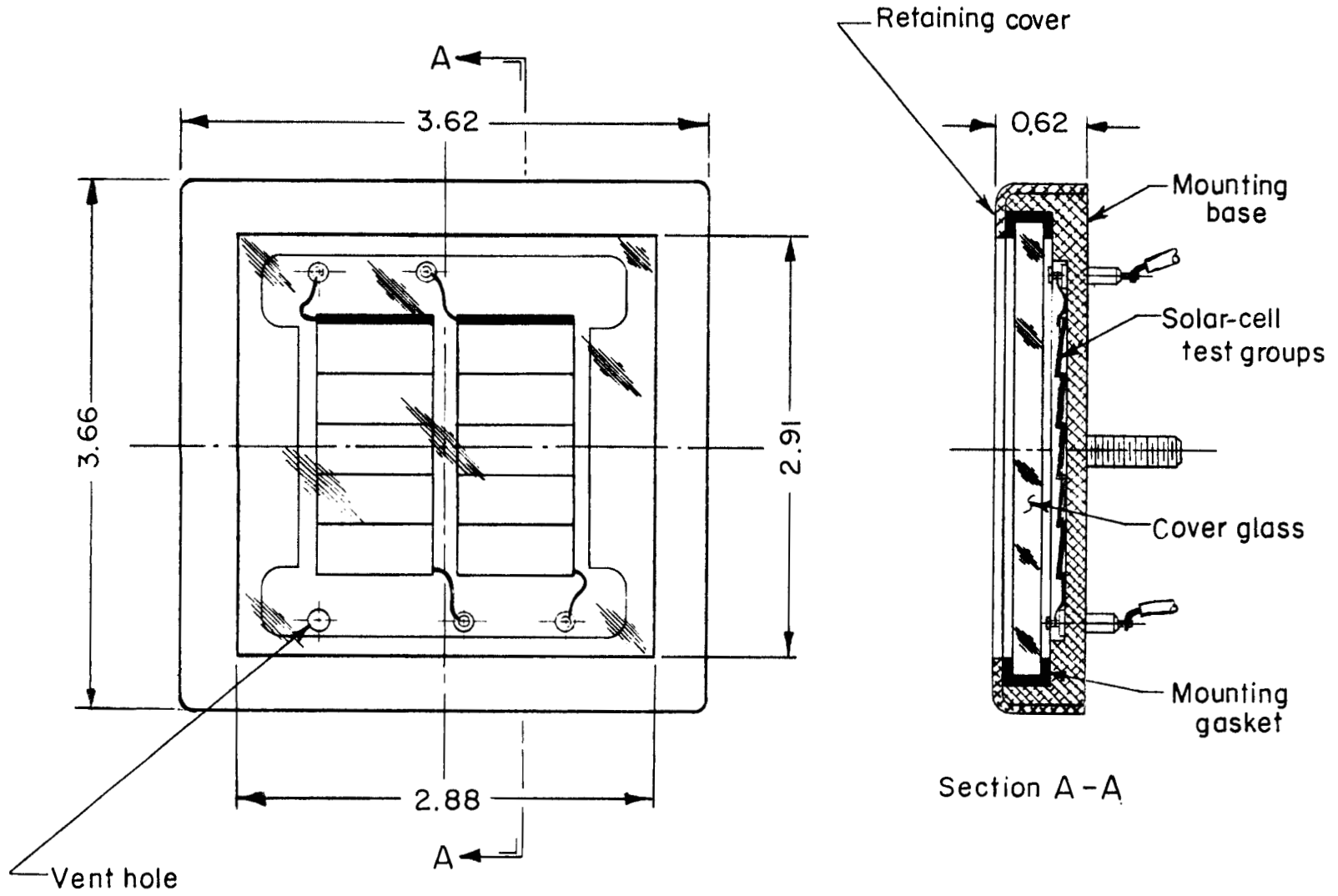

Figure 10.- Test solar cell assembly. All dimensions are in inches.

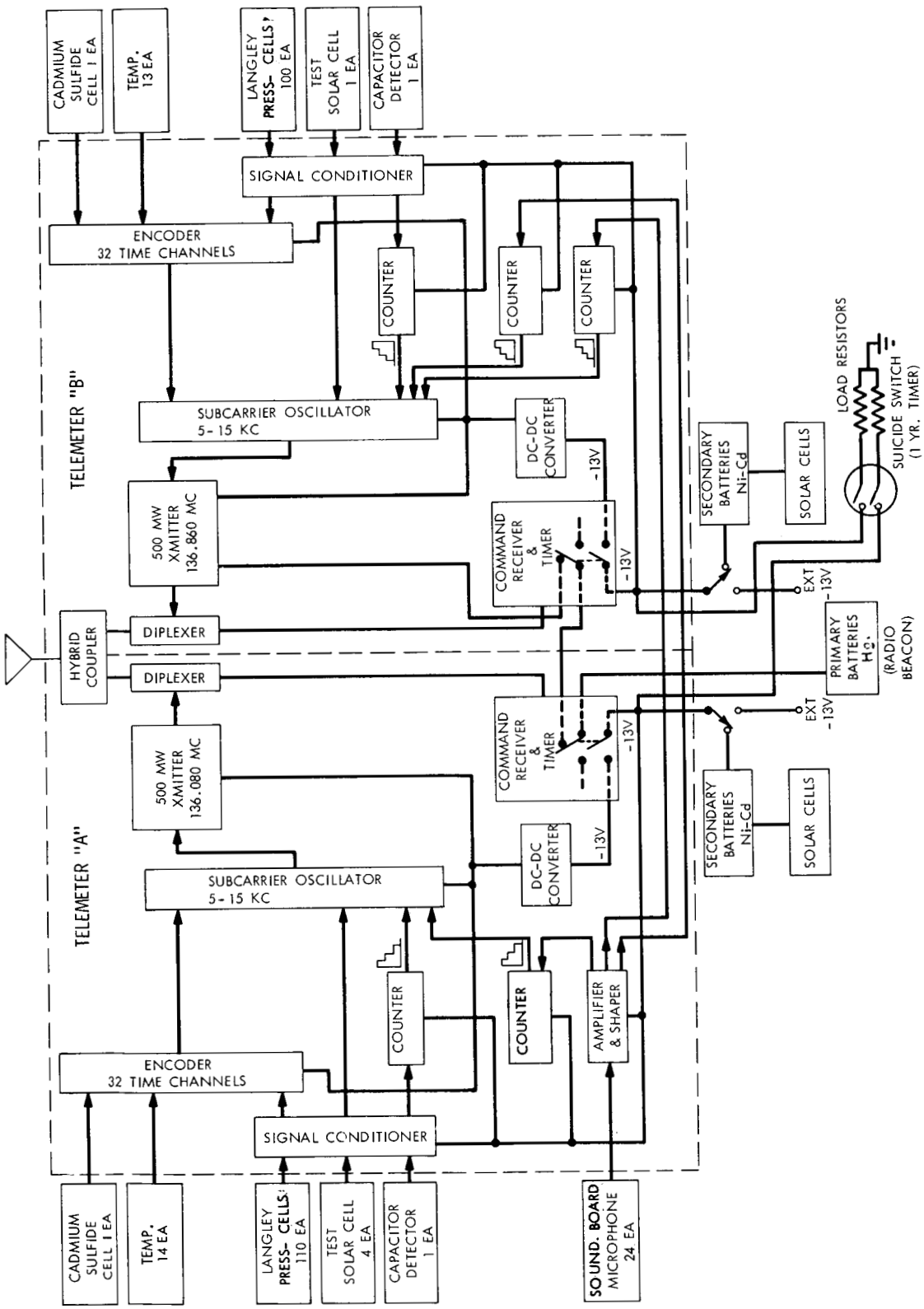

Figure 11.- Block diagram of telemetry system.

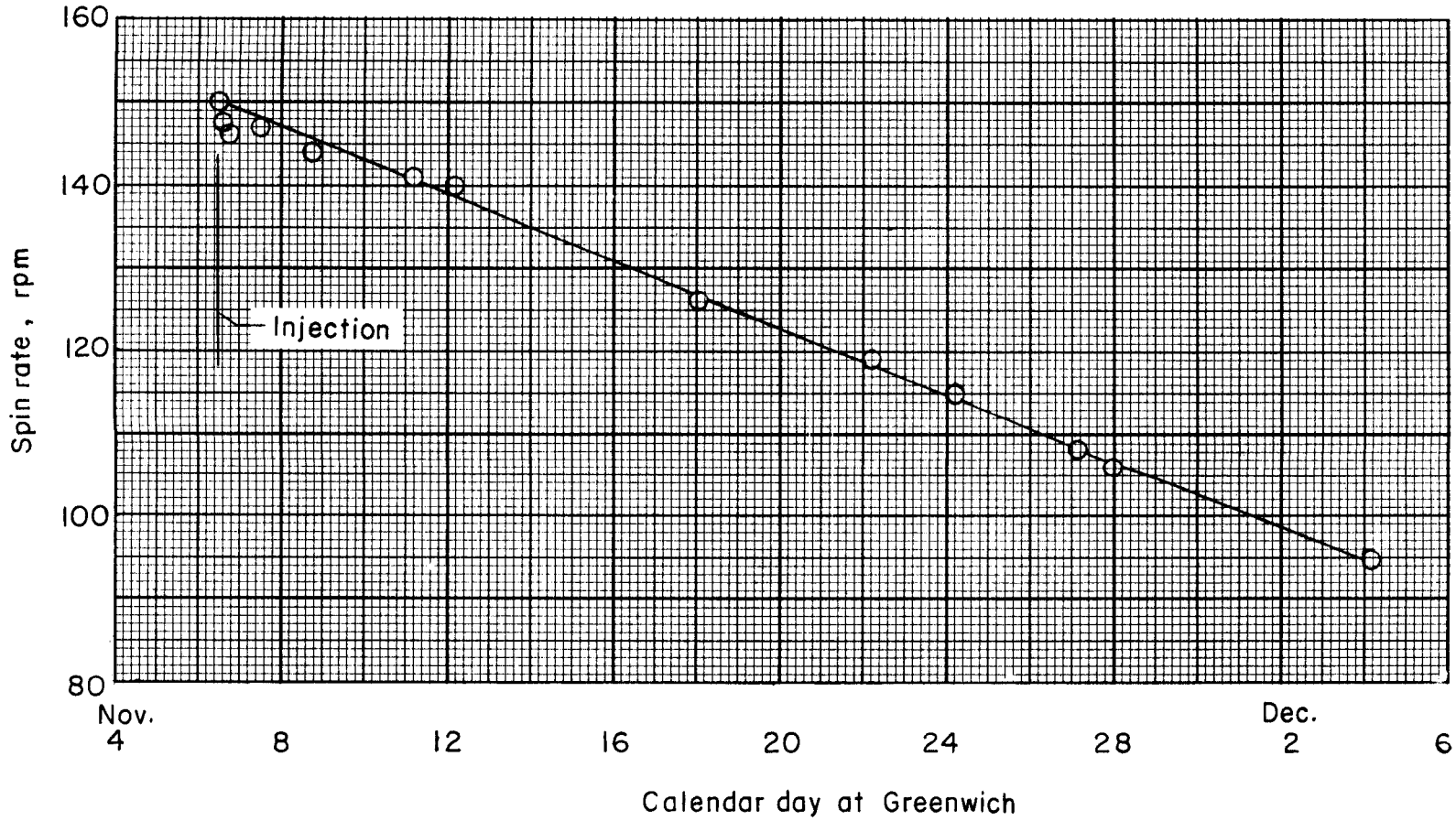

Figure 12.- Spacecraft spin rate since launch.

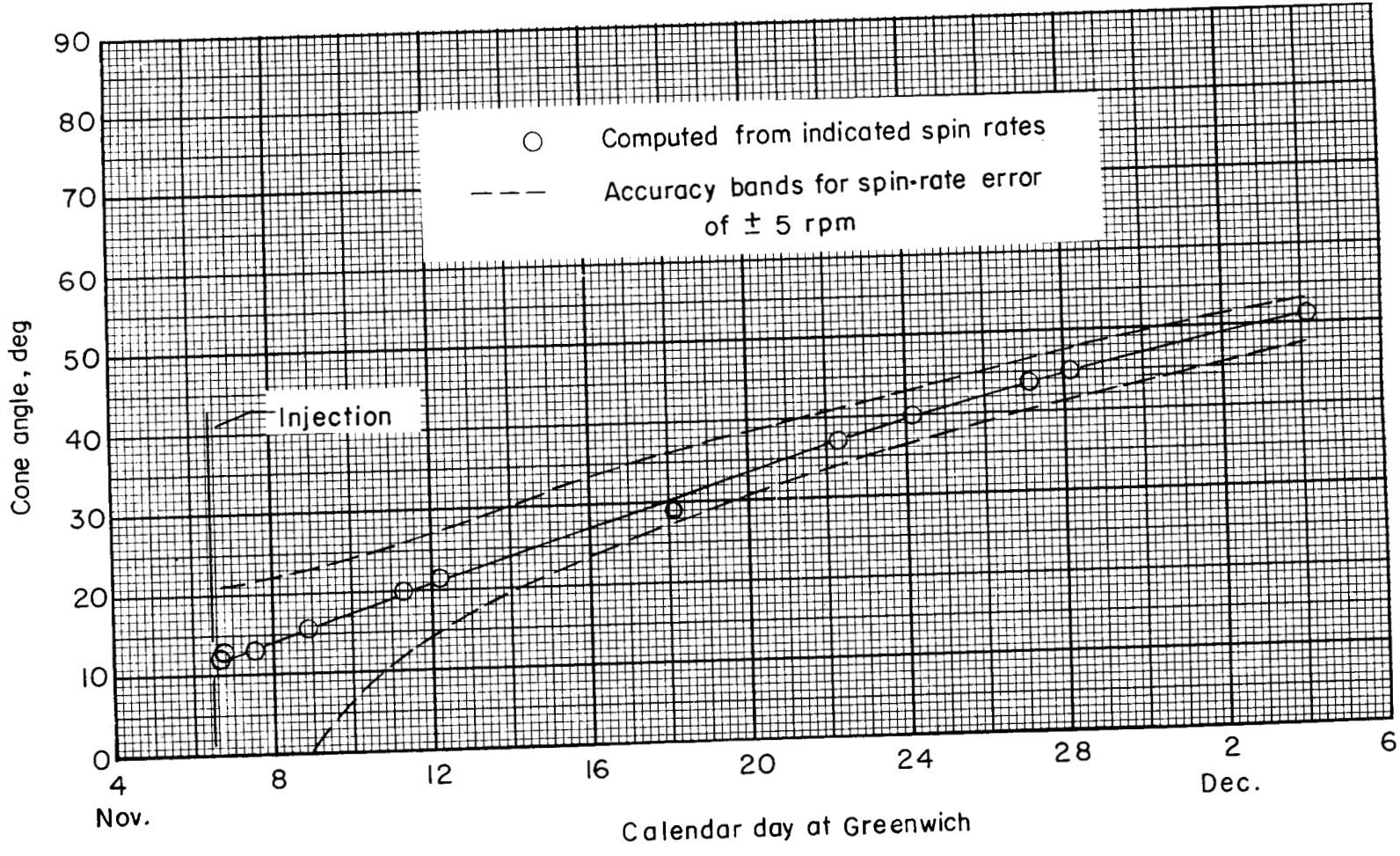

Figure 13.- Spacecraft coning angle since launch.

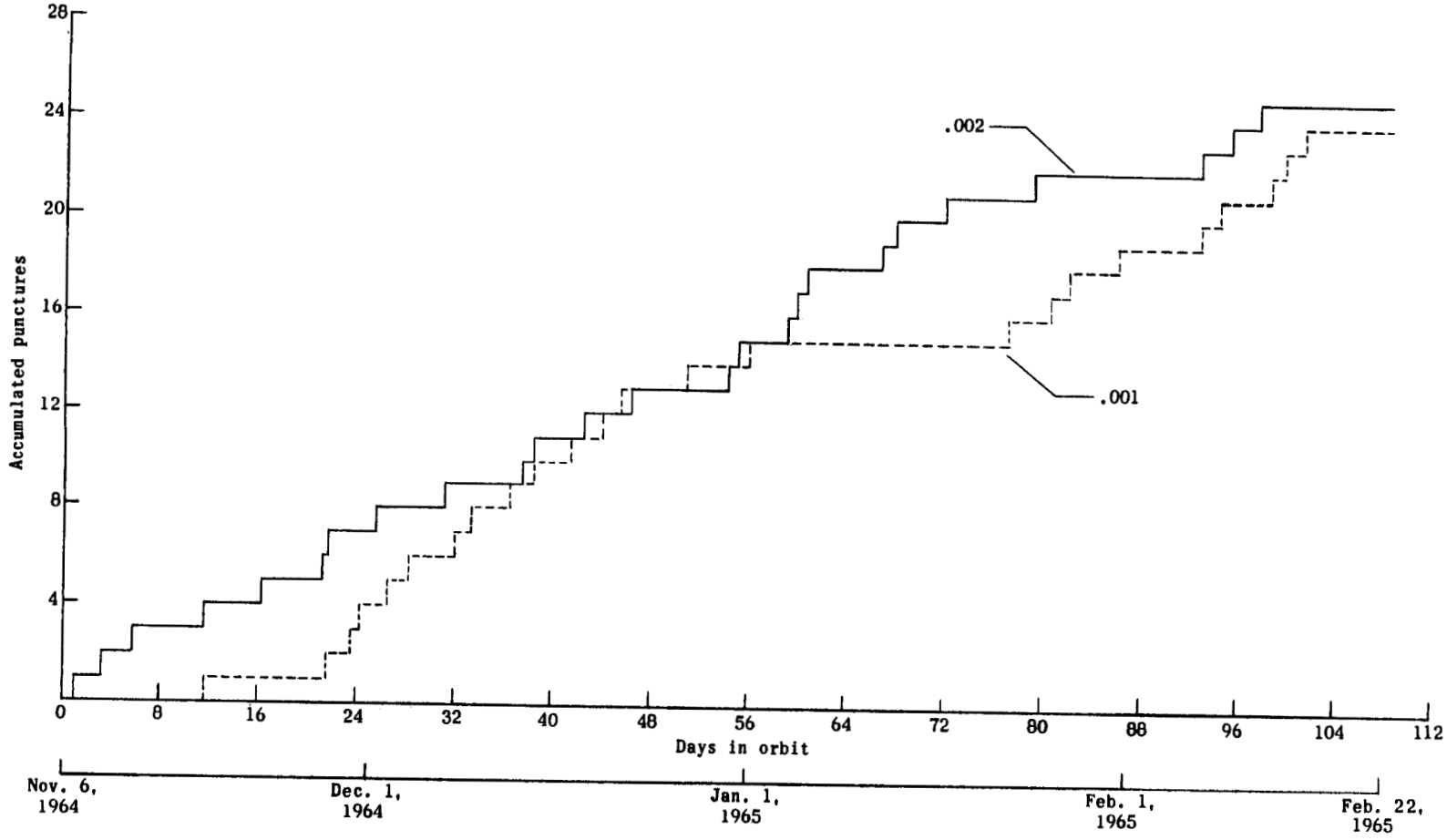

Figure 14.- History of punctures for 0.001- and 0.002-inch sensors.

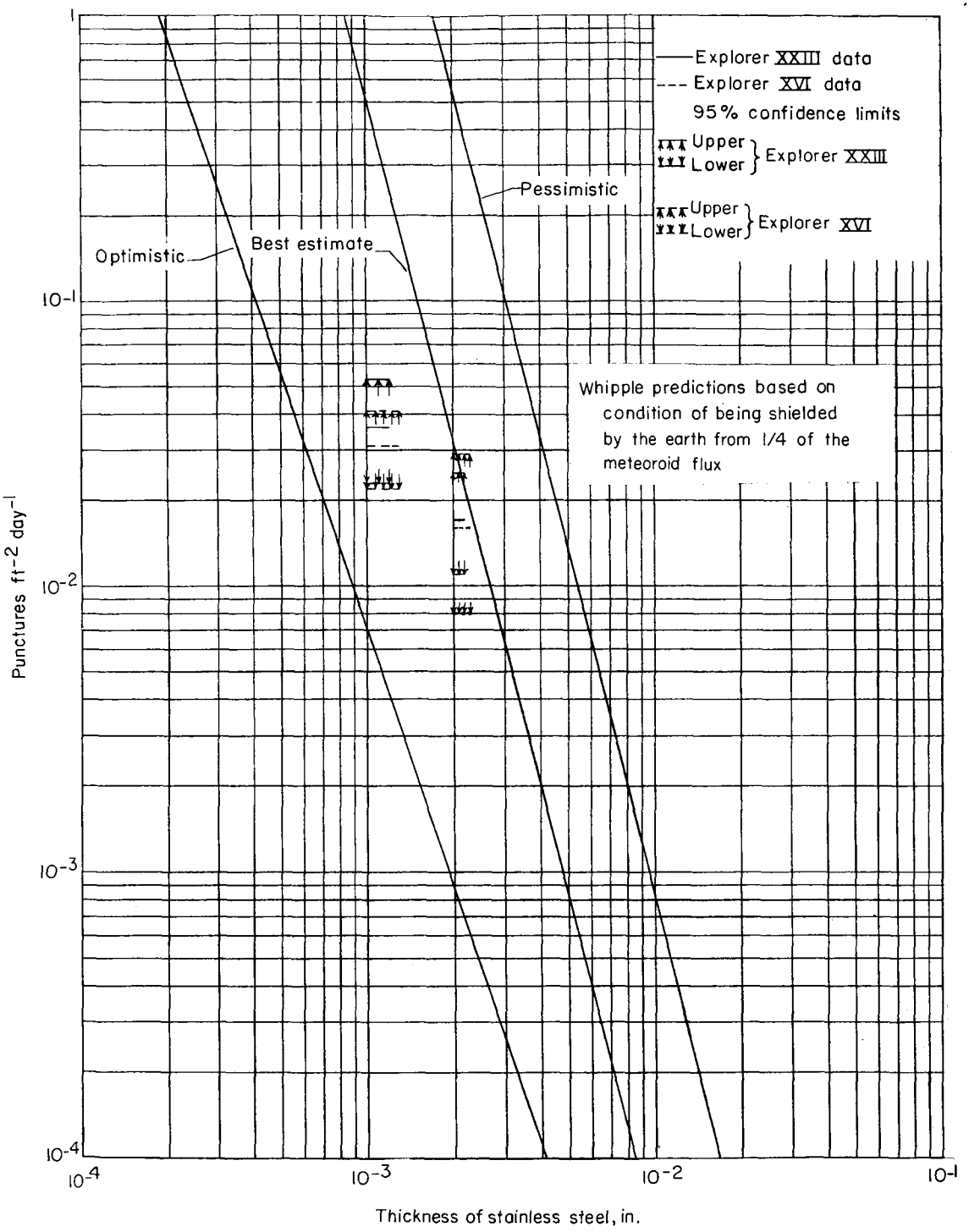

Figure 15.- Comparison of three curves of predicted puncture rate as a function of stainless-steel-sheet thickness with Explorer XVI and Explorer XXIII pressure-cell data. Dashed bars represent data from beryllium-copper cells on Explorer XVI and solid bars represent data from stainless-steel cells on Explorer XXIII, both with 95-percent confidence limits noted.

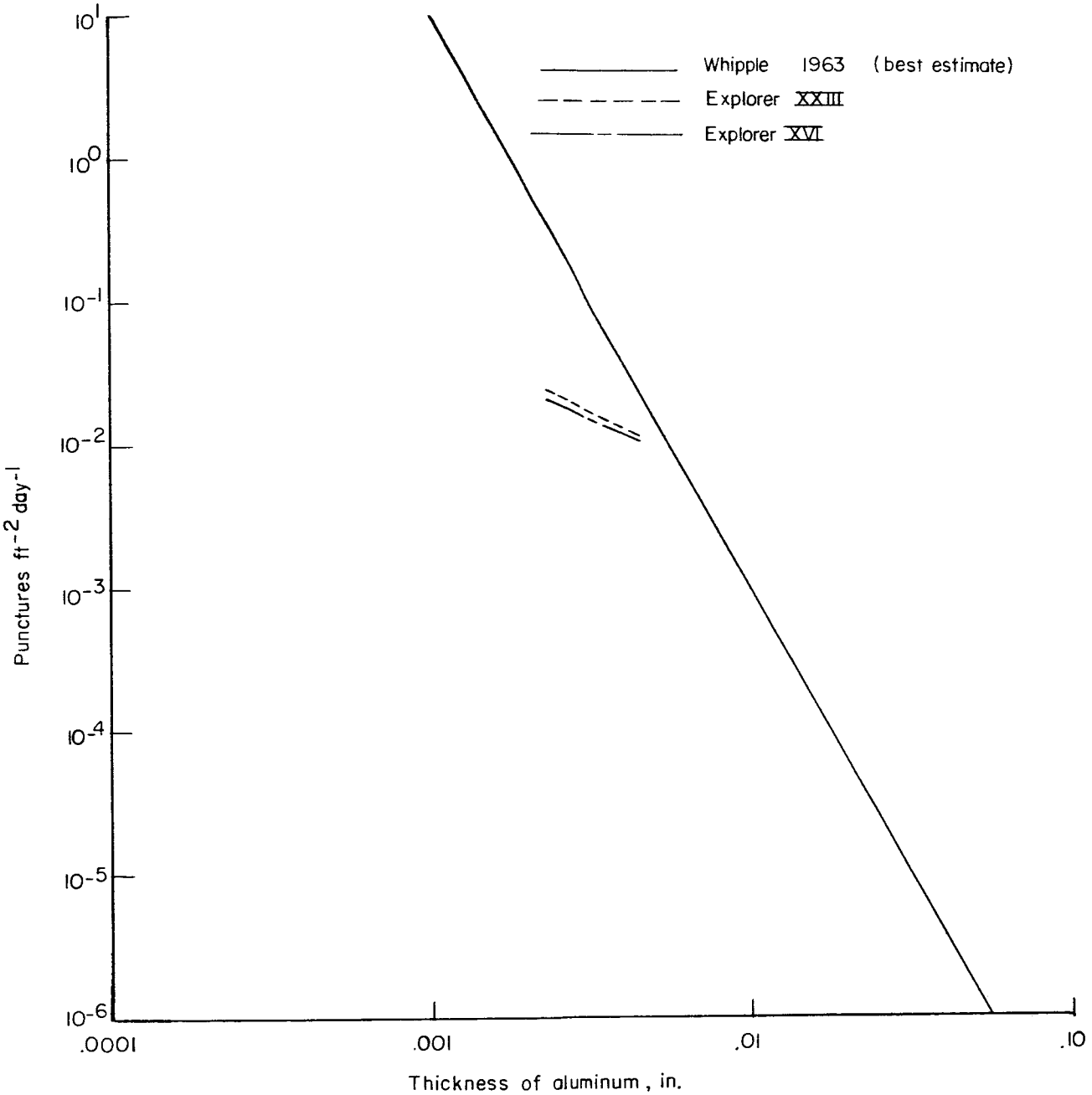

Figure 16.- Predicted puncture rate in aluminum when shielded by earth from one-half of meteoroid flux.

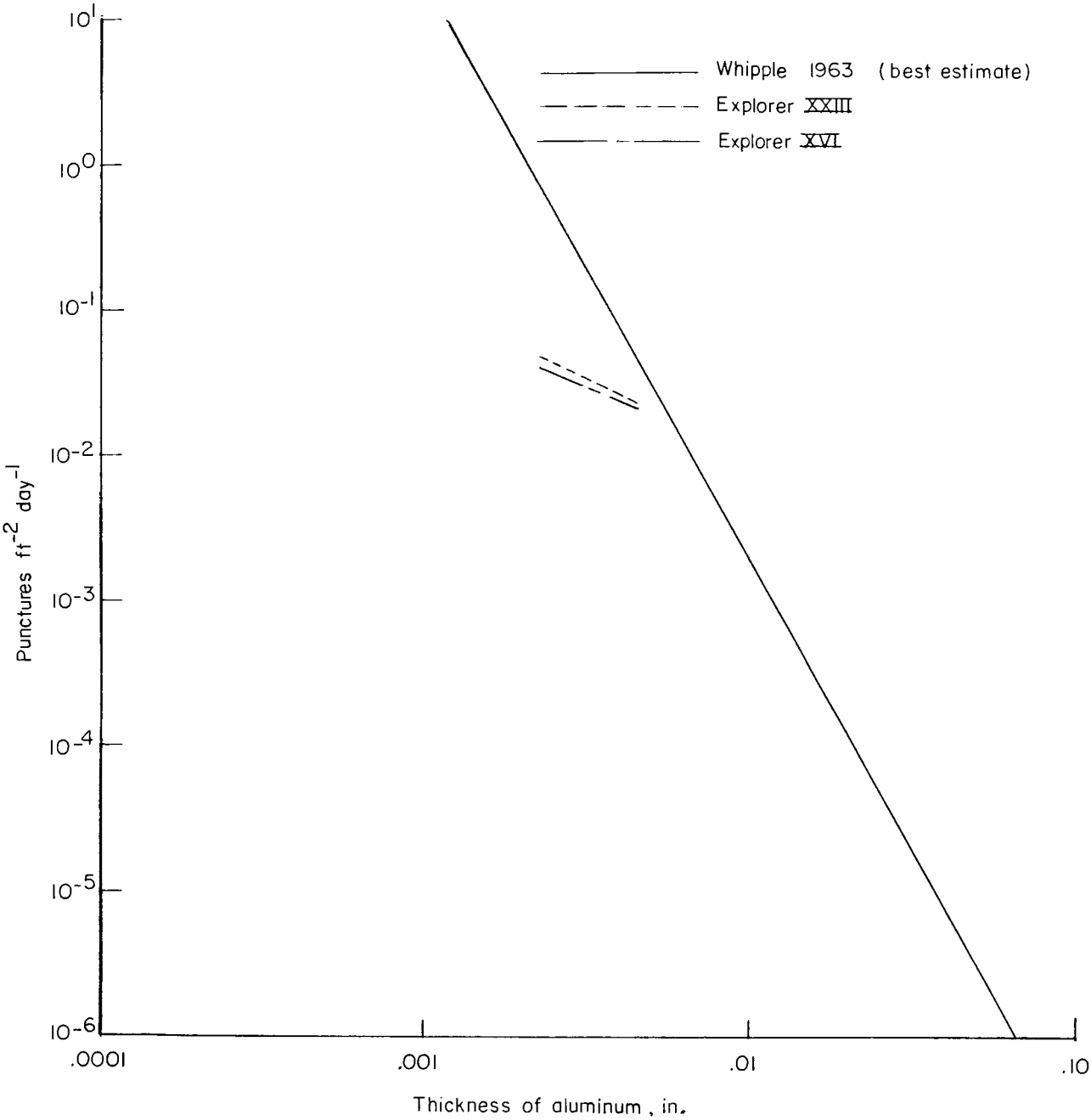

Figure 17.- Predicted puncture rate in aluminum with no earth shielding.

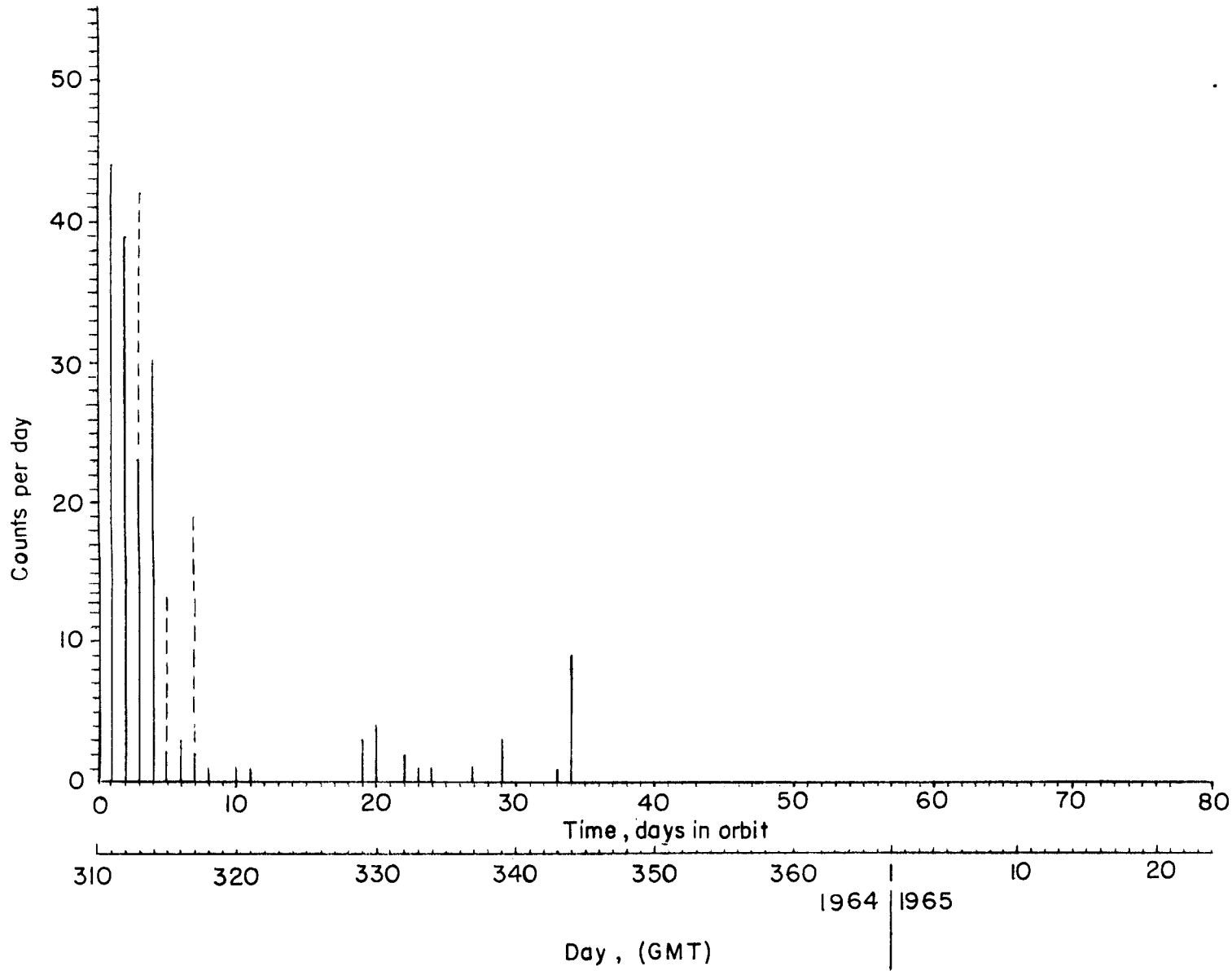

Figure 18.- Daily impact accumulation for high-sensitivity range of meteoroid detection system.

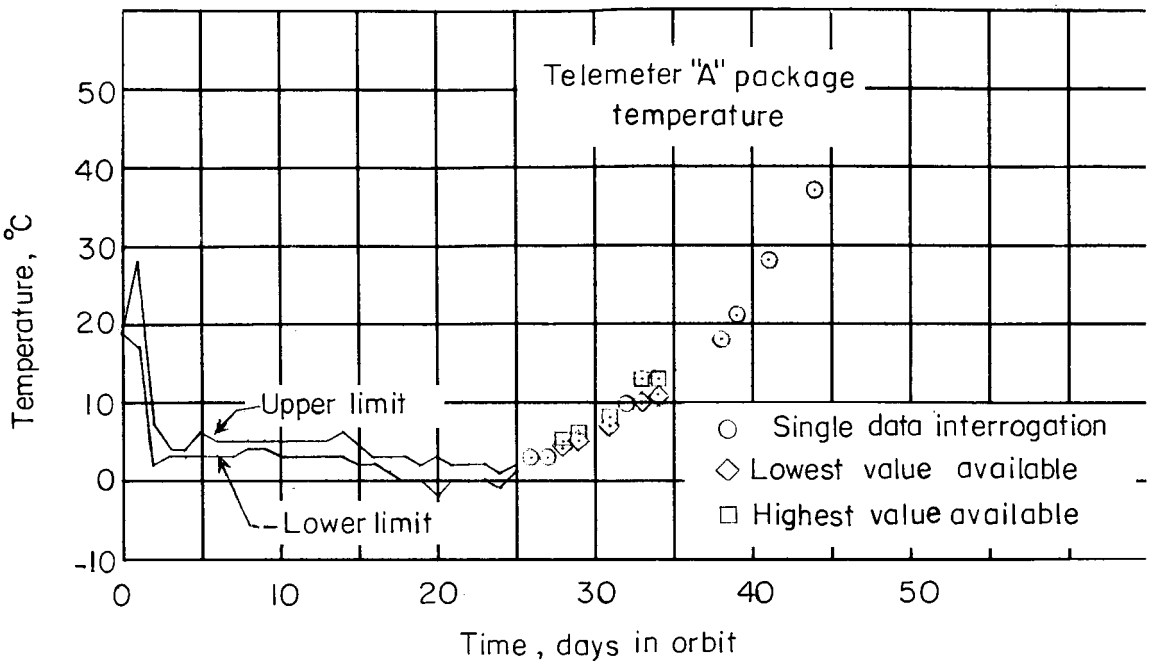

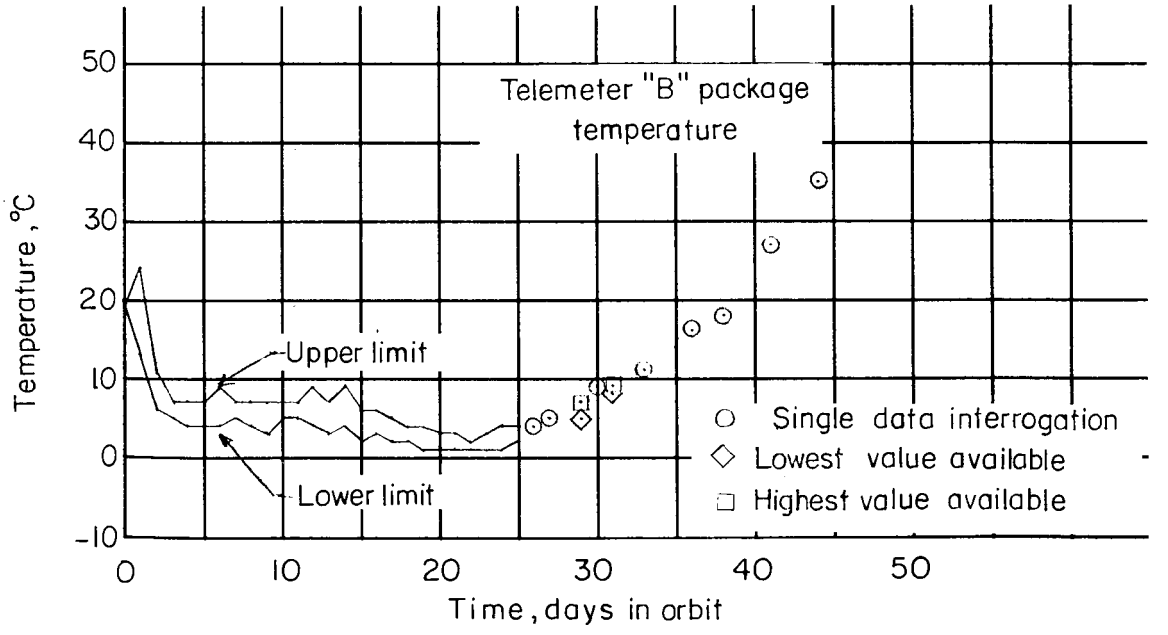

Figure 19.- Temperature history of telemeter package.

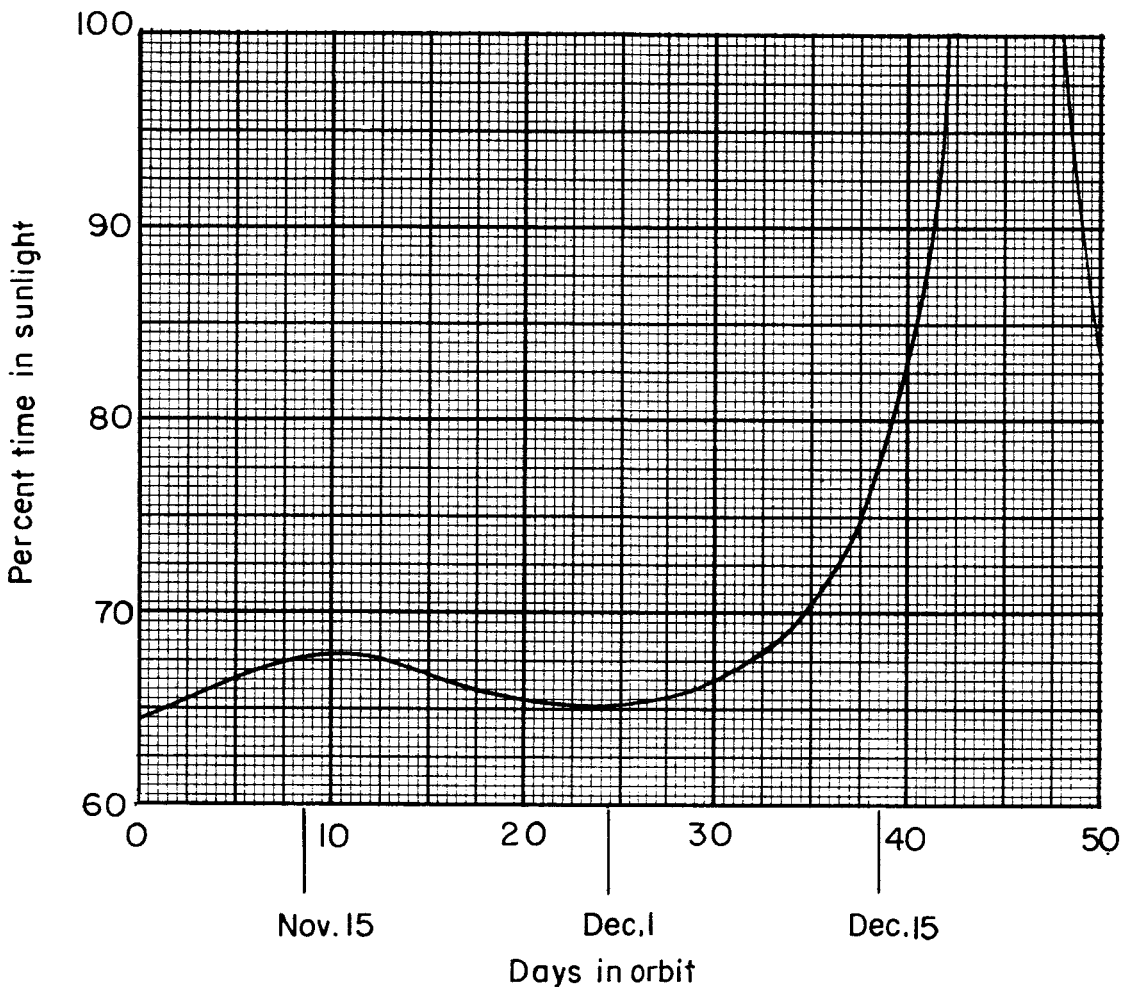

Figure 20.- Explorer XXIII percent time in sunlight (predicted).

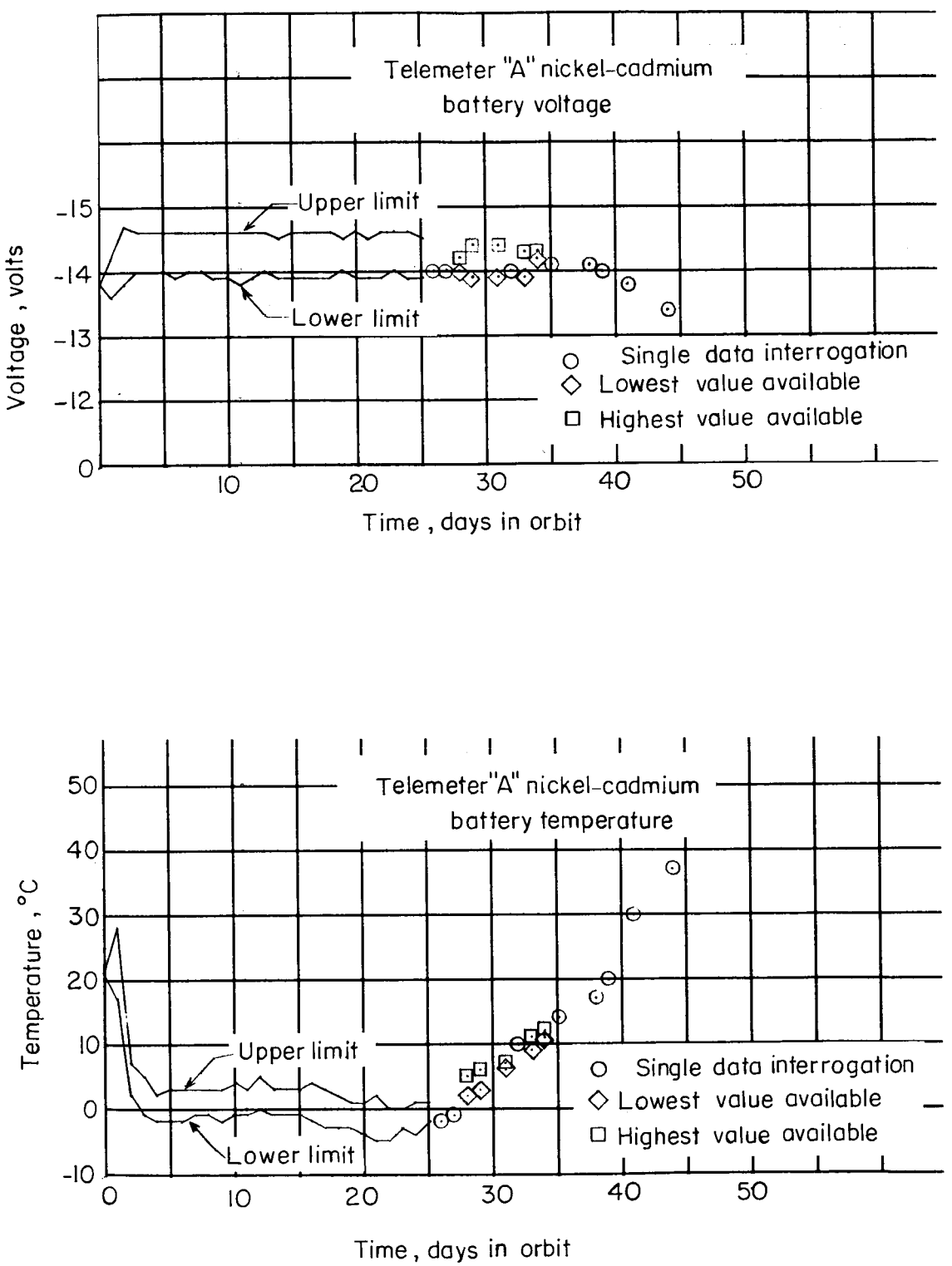

Figure 21.- Nickel-cadmium battery voltage and temperature for telemeter "A."

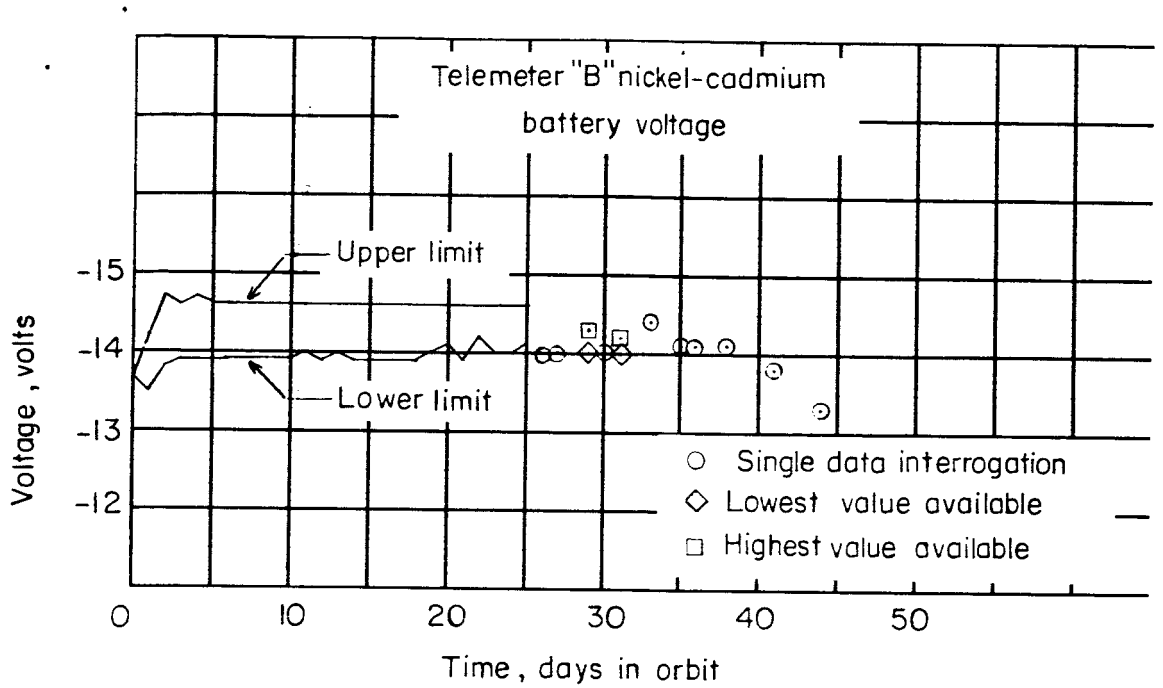

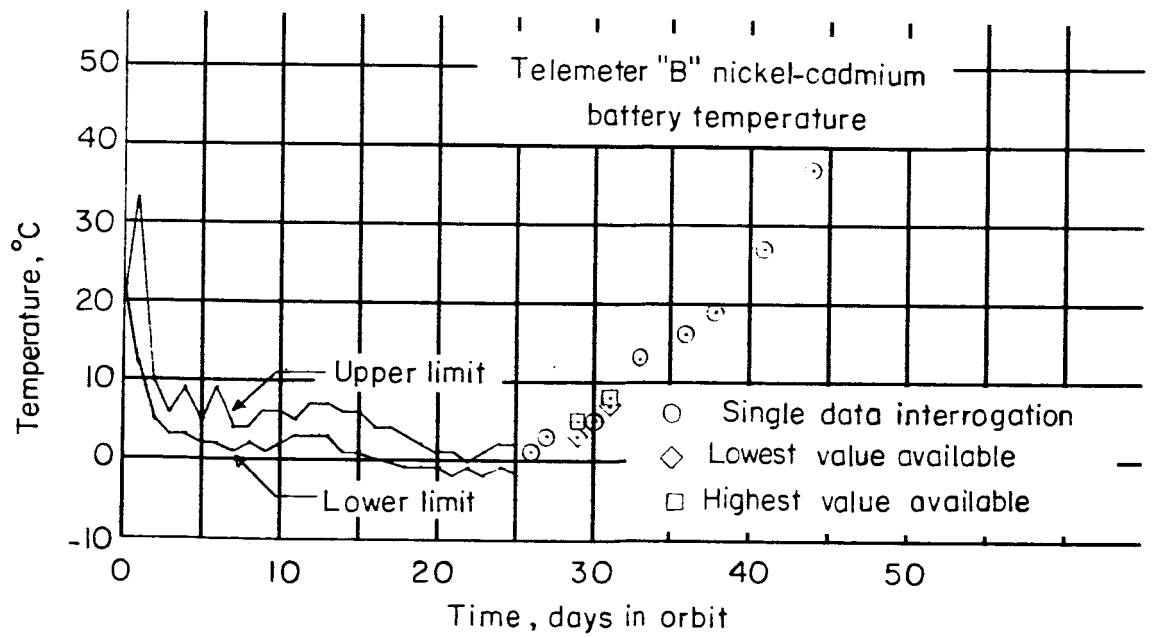

Figure 22.- Nickel-cadmium battery voltage and temperature for telemeter "B."

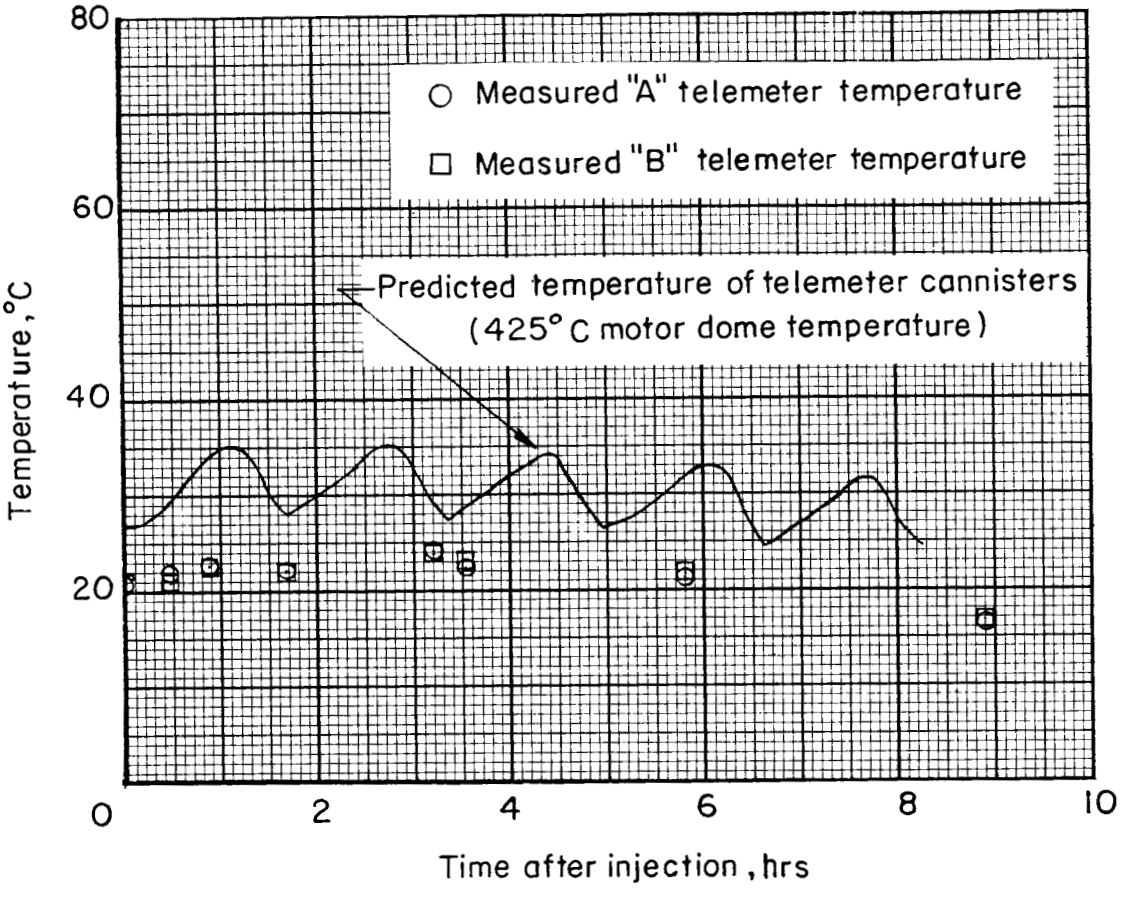

Figure 23.- Predicted and measured telemeter temperatures showing effects of rocket-motor heating.

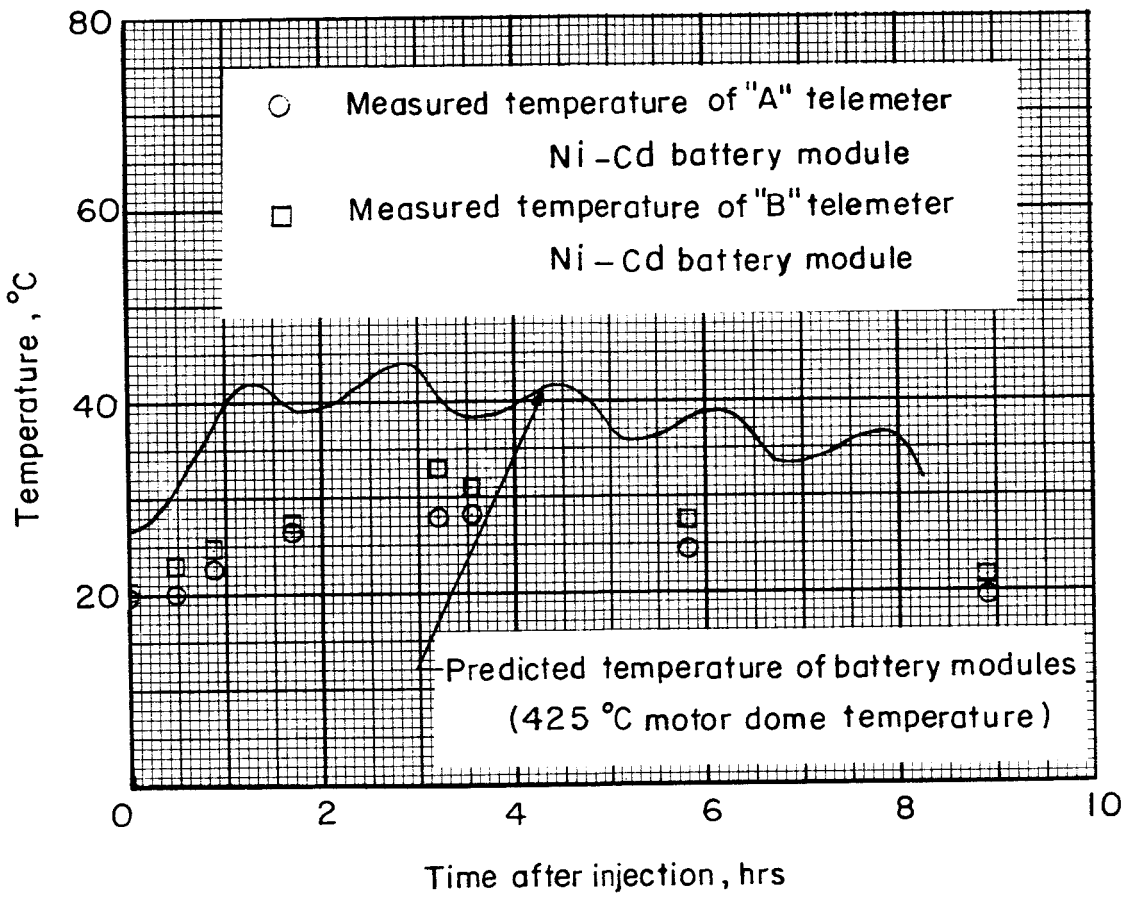

Figure 24.- Predicted and measured battery temperatures showing effects of rocket-motor heating.

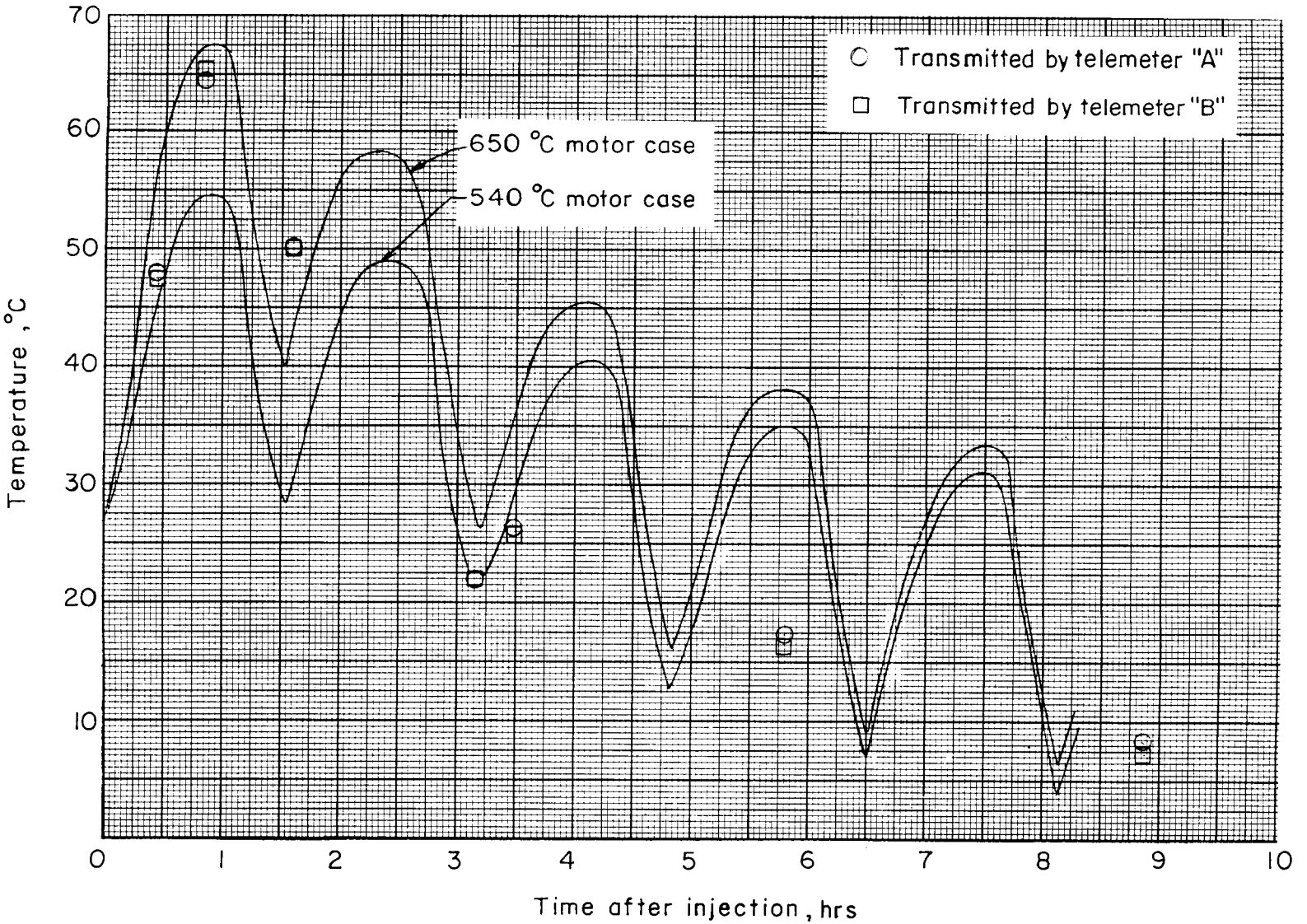

Figure 25.- Predicted and measured temperatures of the fourth row of pressure cells.

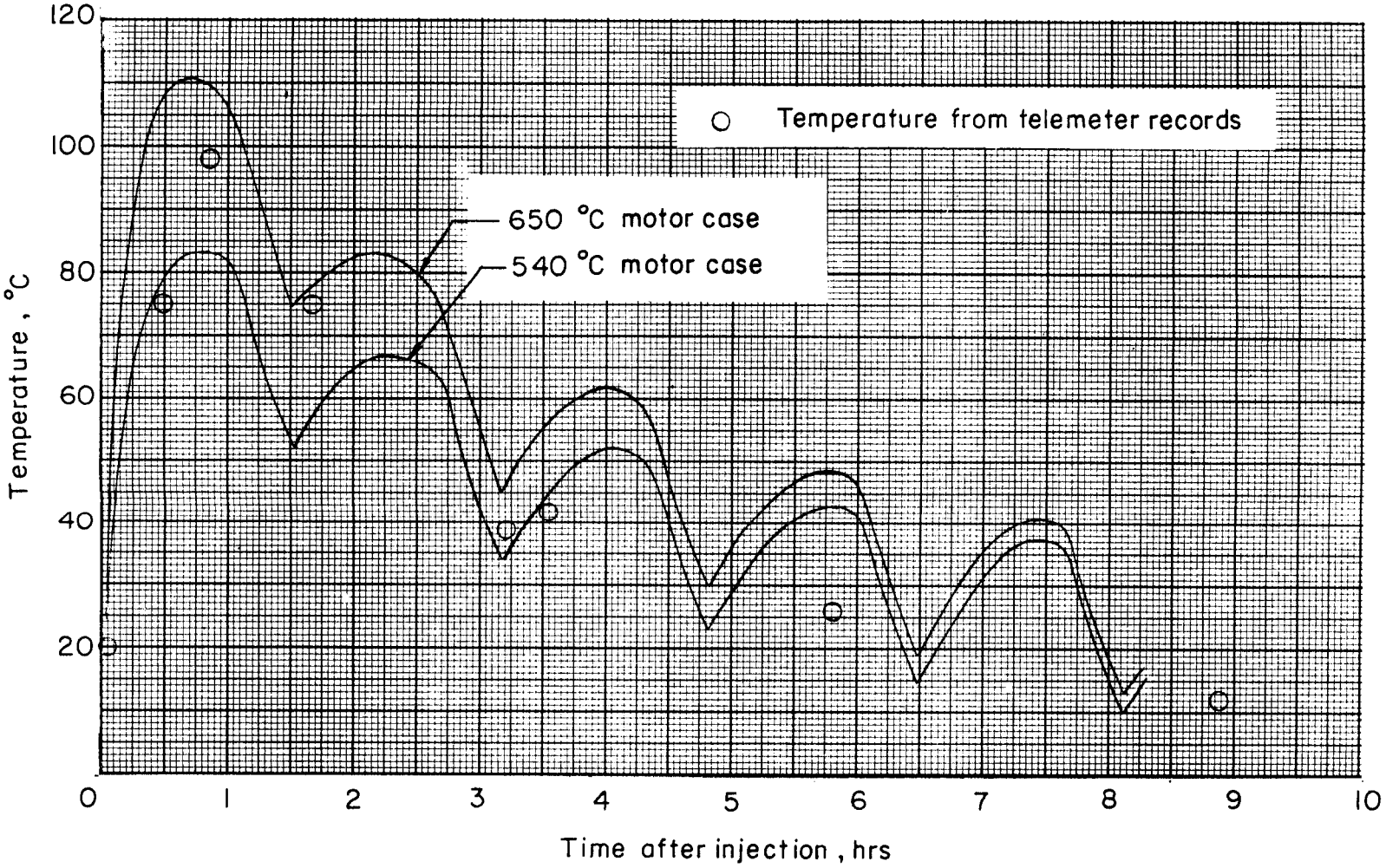

Figure 26.- Predicted and measured temperatures of the sixth row of pressure cells.

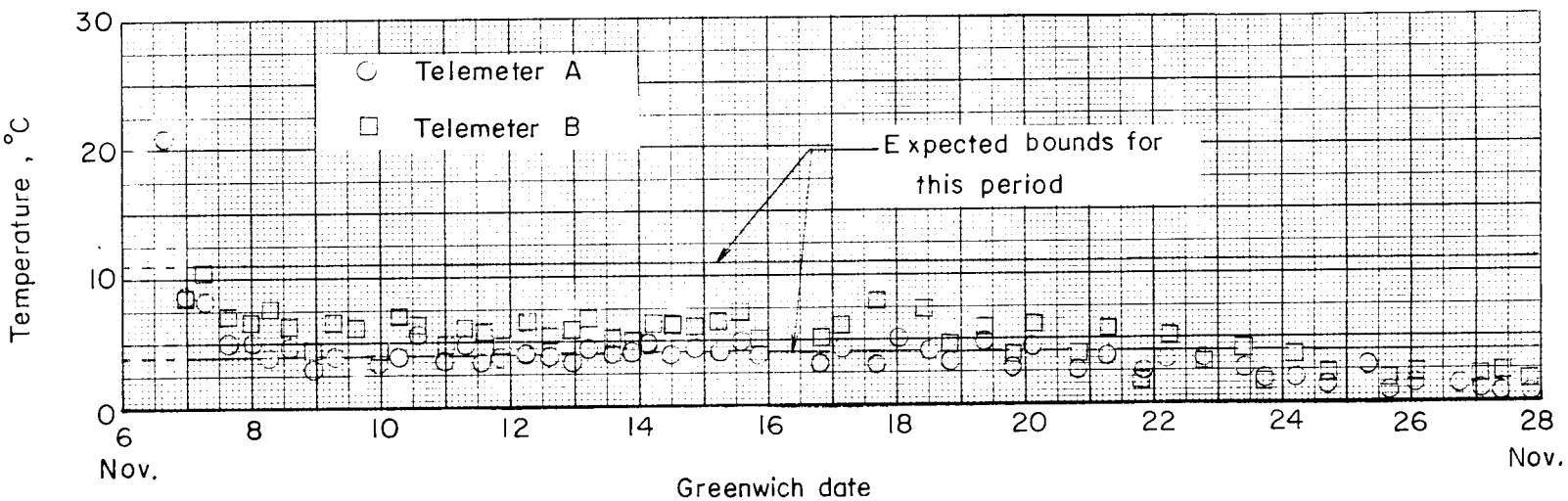

Figure 27.- Telemeter temperature variation with time.

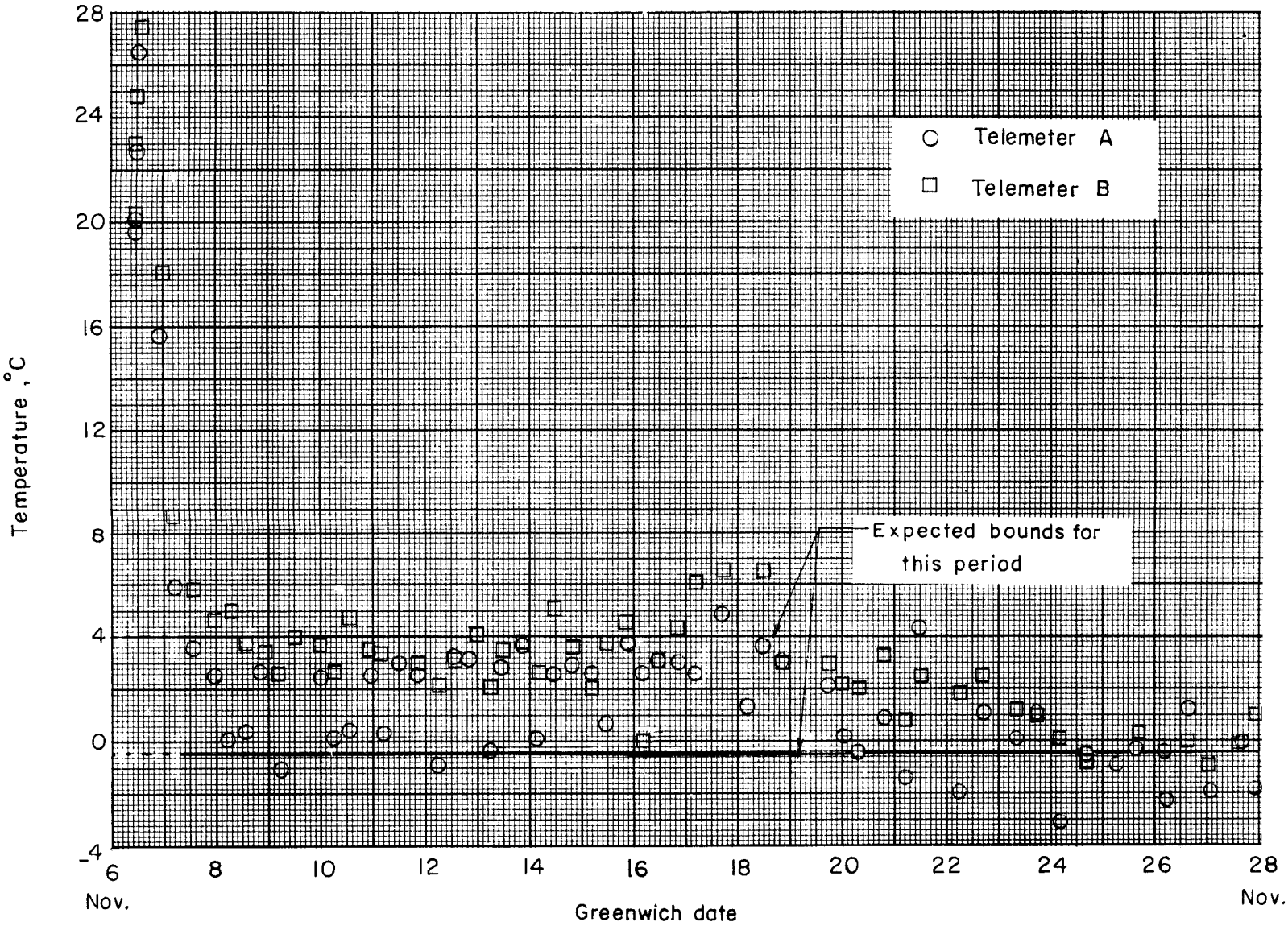

Figure 28.- Battery temperature variation with time.

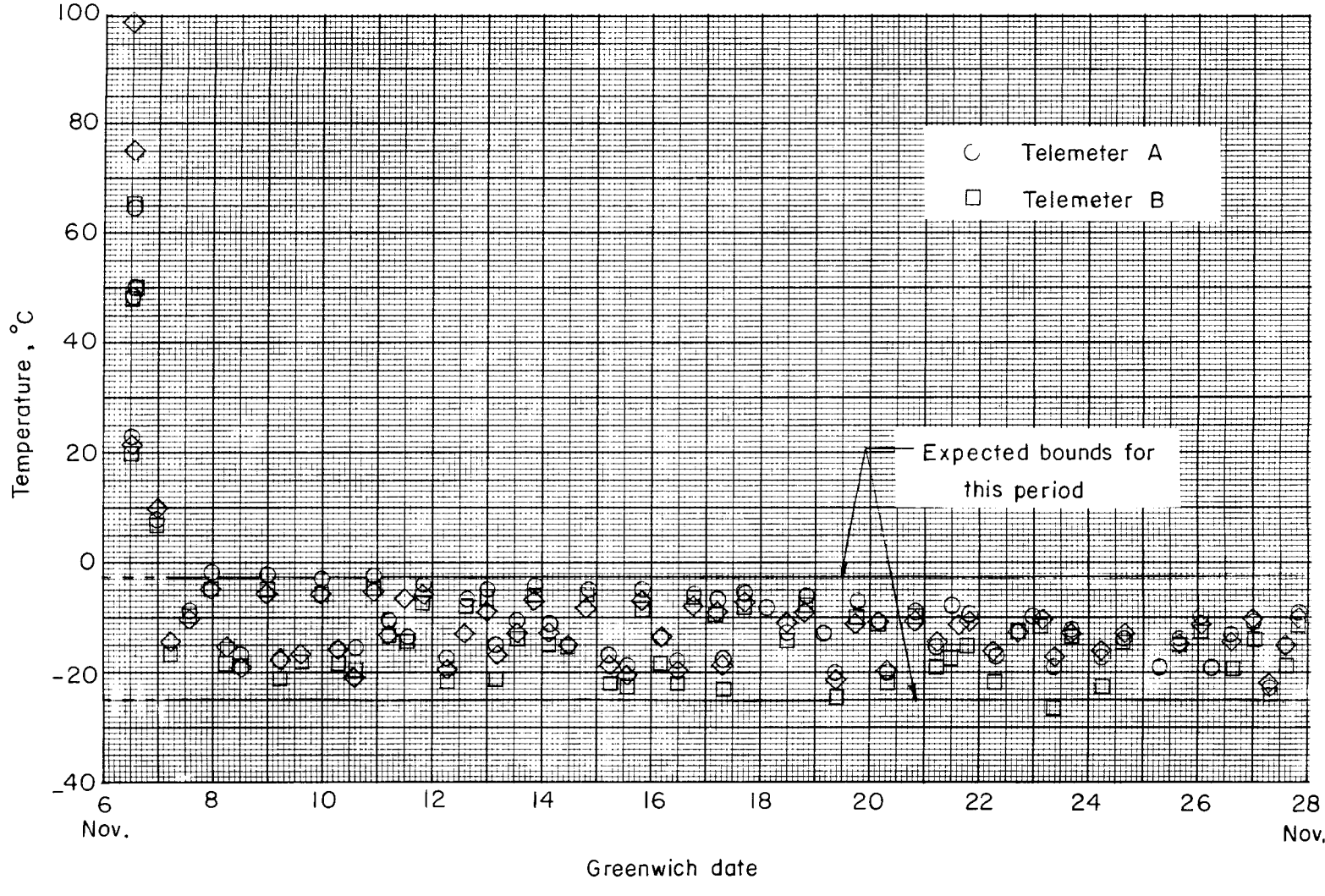

Figure 29.- Pressure-cell temperature variation with time.

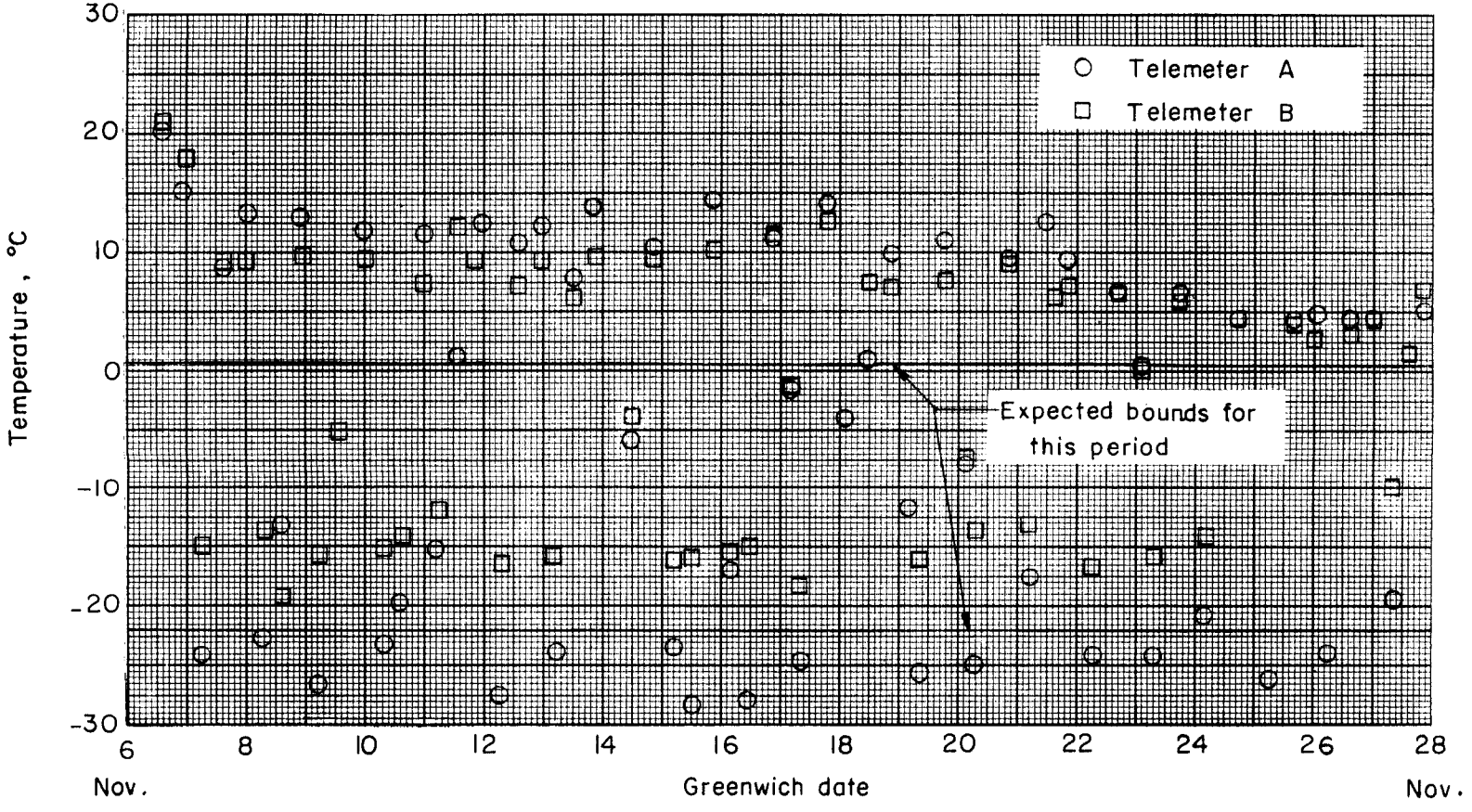

Figure 30.- Capacitor detector temperature variation with time.

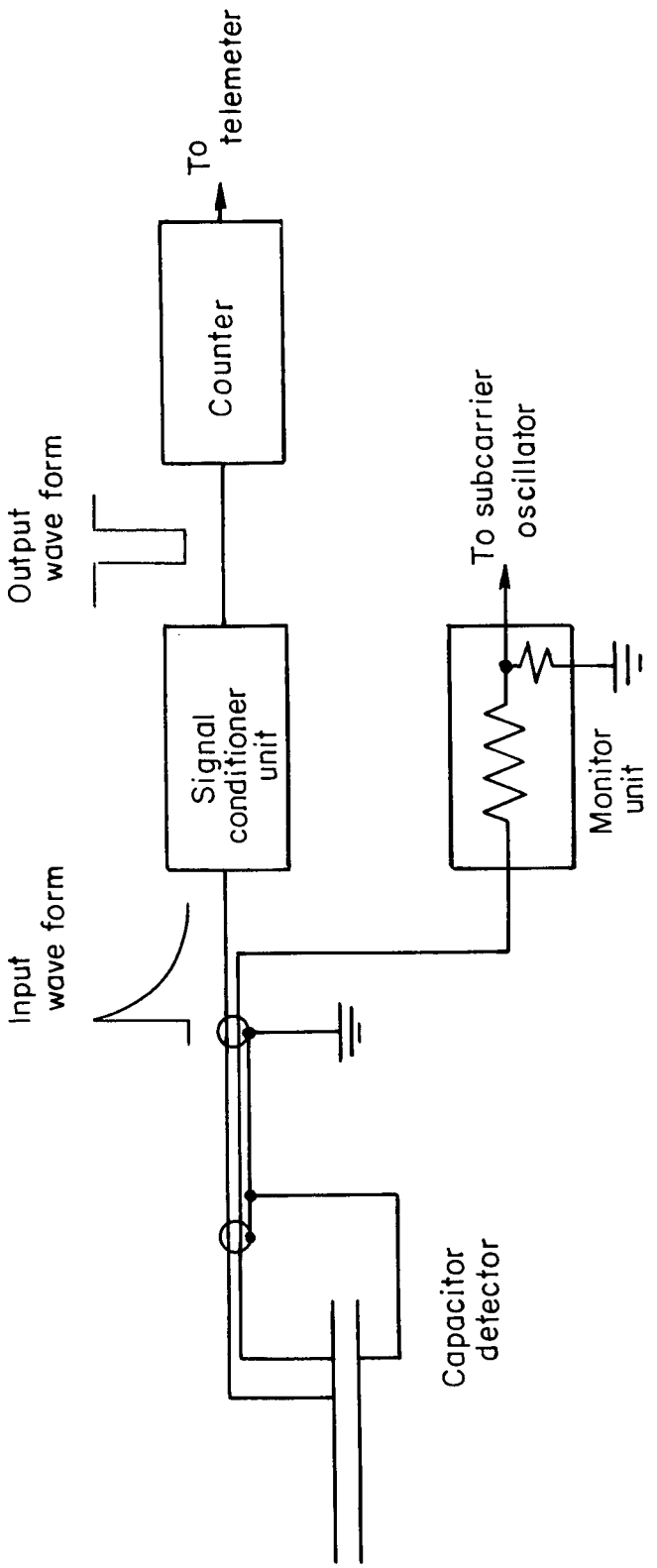

Figure 31.- Block diagram of capacitor-detector circuitry.

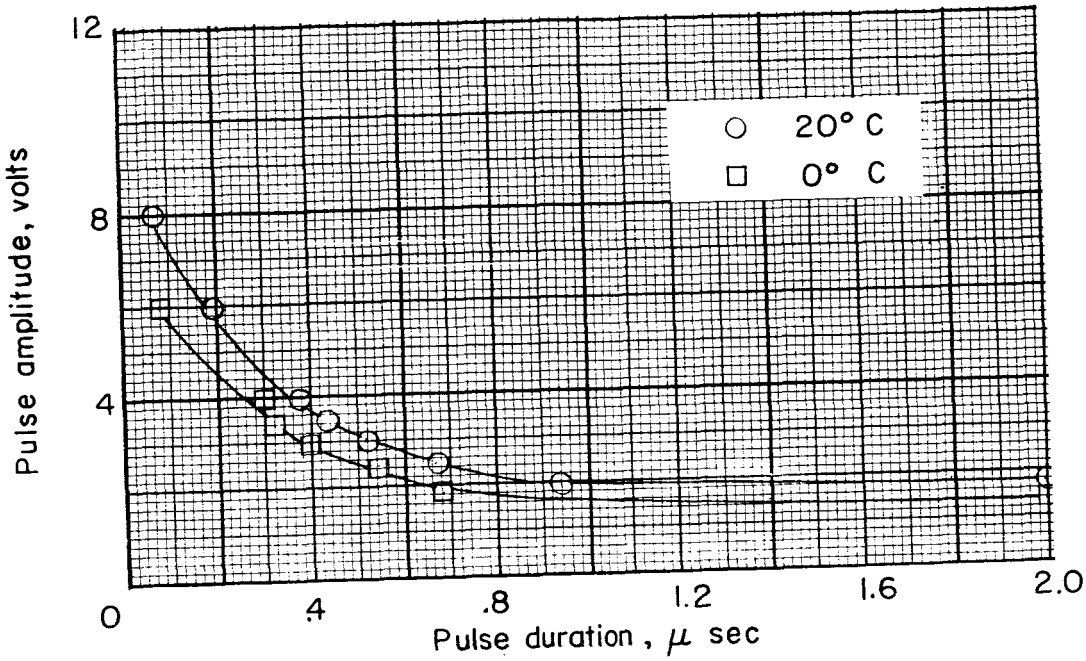

(a) Calibration for "A" detector-signal conditioning unit.

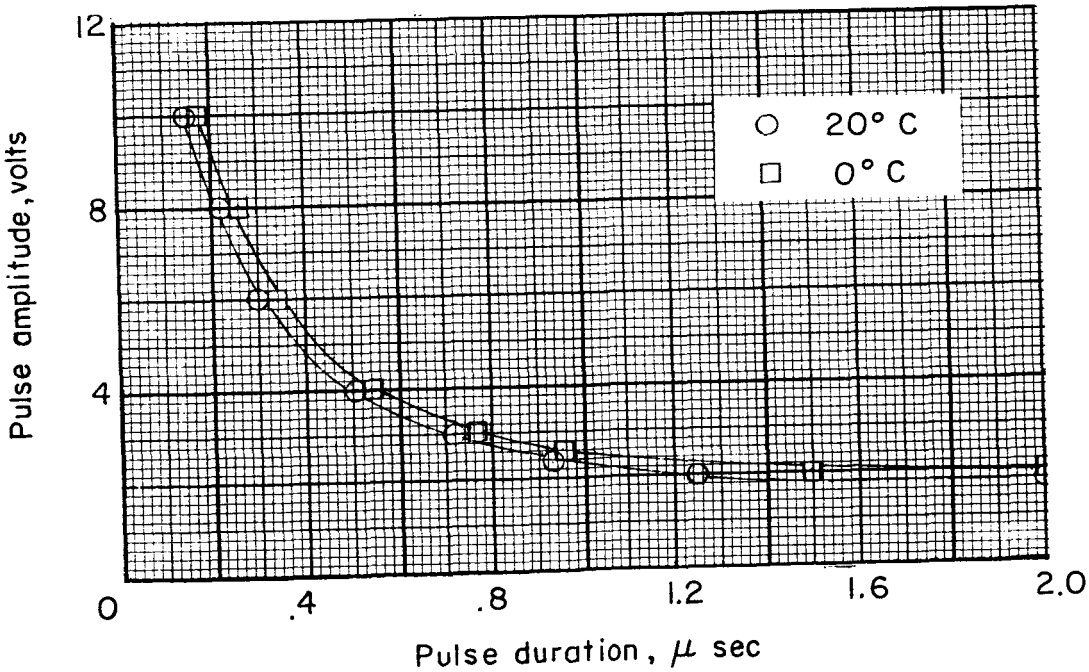

(b) Calibration for "B" detector-signal conditioning unit.

Figure 32.- Calibration of capacitor-detector signal conditioning units.

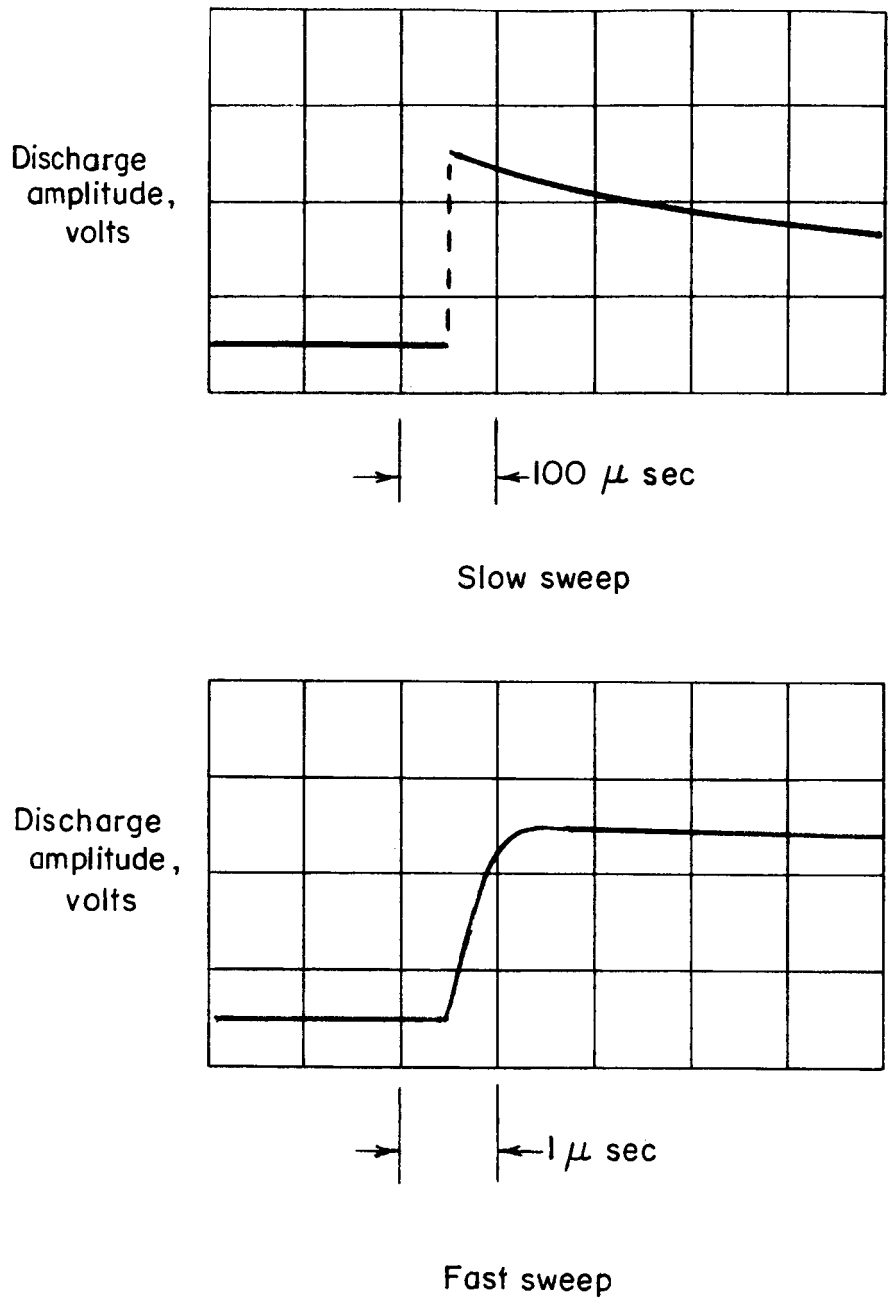

Figure 33.- Typical capacitor-detector discharge wave form from a hypervelocity projectile penetration (from oscilloscope photograph).

NASA-Langley, 1965 L-4549